

The evolution of the heaviest super-massive black-holes in jetted AGNs

Diana A.,^{1,2*} Caccianiga A.,^{2†} Ighina L.,^{2,3} Belladitta S.,^{2,3} Moretti A.,² Della Ceca R.²

¹*Dipartimento di Fisica G. Occhialini, Università di Milano-Bicocca, Piazza della Scienza 3, 20126 Milano, Italy*

²*INAF - Osservatorio Astronomico di Brera, via Brera 28, I-20121 Milan, Italy*

³*DiSAT, Università degli Studi dell'Insubria, Via Valleggio 11, 22100, Como, Italy*

Accepted XXX. Received YYY; in original form ZZZ

ABSTRACT

We present the space density evolution, from $z=1.5$ up to $z=5.5$, of the most massive ($M \geq 10^9 M_\odot$) black holes hosted in jetted *Active Galactic Nuclei* (AGNs). The analysis is based on a sample of 380 luminosity-selected ($\lambda L_{1350} \geq 10^{46}$ erg s $^{-1}$ and $P_{5\text{GHz}} \geq 10^{27}$ W Hz $^{-1}$) Flat Spectrum Radio Quasars (FSRQs) obtained from the *Cosmic Lens All Sky Survey* (CLASS). These sources are known to be face-on jetted AGNs (i.e. blazars) and can be exploited to infer the abundance of all the (misaligned) jetted AGNs, using a geometrical argument. We then compare the space density of the most massive SMBHs hosted in jetted AGNs with those present in the total population (mostly composed by non-jetted AGNs). We find that the space density has a peak at $z \sim 3$, which is significantly larger than the value observed in the total AGN population with similar optical/UV luminosities ($z \sim 2.2$), but not as extreme as the value previously inferred from X-ray selected blazars ($z \gtrsim 4$). The jetted fraction (jetted AGNs/total AGNs) is overall consistent with the estimates in the local Universe (10–20%) and at high redshift, assuming Lorentz bulk factors $\Gamma \approx 5$. Finally, we find a marginal decrease in the jetted fraction at high redshifts (by a factor of ~ 2). All these evidences point toward a different evolutionary path in the jetted AGNs compared to the total AGN population.

Key words: quasars: supermassive black holes – galaxies: active

1 INTRODUCTION

Studying how Super-Massive Black Holes (SMBHs) have evolved across cosmic time is a fundamental step for our comprehension of the formation and evolution of the cosmic structures in the Universe. According to the current paradigm, the growth of the SMBH should happen during the process of accretion on a massive black hole seed present in the centre of a galaxy (e.g. Merloni 2016 for a comprehensive review). Since the accretion is also the basis of the AGN phenomenon, tracing the evolution of the AGN phase represents the most compelling way to study the SMBHs growth, especially at high redshifts (e.g. Volonteri 2010; Valiante et al. 2017). Particularly important is to establish the possible role of relativistic jets in this process (for a recent review on the relativistic jets in AGNs see Blandford et al. 2019). These powerful and collimated jets are able to produce strong radio emission and hence the jetted AGNs are usually referred as radio-loud (RL, e.g. Best & Heckman 2012). If the presence of a jet is the consequence of a rapidly spinning black hole (e.g. Tchekhovskoy et al. 2011; Narayan et al. 2014), we expect that RL AGNs should be very effective in transforming accreting mass into energy (Tchekhovskoy et al. 2011; Narayan et al. 2014).

A pure general relativity estimate results in a radiation efficiency of $\eta \sim 0.3$ for a maximal rotating BH and $\eta \sim 0.1$ for a non-rotating BH (e.g. Thorne 1974). Therefore the black hole mass-growth in RL AGNs should be on average significantly slower compared to non-jetted, or radio-quiet (RQ), AGNs. As a consequence, we expect the most massive SMBHs hosted in RL to be less abundant at high redshift than those hosted in the RQ counterpart, assuming that RL AGNs remain that way through all their accretion episodes. Evidence supporting this prediction, however, has not been found yet. On the contrary, several studies have shown no clear dependence on the ratio of RL to RQ AGNs with redshift (e.g. Stern et al. 2000; Bañados et al. 2015; Liu et al. 2021) while other studies indicate that RL AGNs with the most massive SMBHs ($\geq 10^9 M_\odot$) show a more rapid evolution, peaking earlier ($z \gtrsim 4$; e.g. Ajello et al. 2009; Sbarato et al. 2015) than those hosted in RQ AGNs (peaking at $z \sim 2$, e.g. Hopkins et al. 2007; Shen et al. 2020).

Establishing if SMBHs hosted in jetted AGNs followed a different evolutionary path compared to those hosted by non-jetted AGNs is not simple. The presence of a relativistic jet is usually inferred from the detection of a strong radio emission that reveals the radio-loud nature of an AGN (e.g. Urry & Padovani 1995). A major problem, however, is that in RL AGNs the radio emission produced by the jet is strongly dependent to the viewing angle, due to relativistic beaming, and, therefore, the same source will show a different

* a.diana3@campus.unimib.it

† alessandro.caccianiga@inaf.it

2 Diana et al.

value of radio-loudness (defined as the rest-frame radio-to-optical luminosity ratio, Kellermann et al. 1989) depending to its actual orientation. This is particularly true at high radio frequencies where the emission is almost completely dominated by the beamed part of the radio emission (the jet). In this respect, high- z AGNs could be very problematic since the typical observing radio frequencies (1.4–5 GHz) correspond to very high rest-frame frequencies (8–30 GHz for a $z=5$ AGN). In addition, the extended (and more isotropic) radio emission from the radio-lobes of RL AGNs could be heavily damped at high- z due to the increasing density of photons from the Cosmic Microwave Background (CMB) that interact and cool the relativistic electrons responsible for the radio emission (Ghisellini et al. 2014a). Finally, as in radio-quiet AGNs, obscuration of the optical/UV radiation, due to the molecular torus, makes the detection of an important fraction of sources (the so-called type-II AGNs) at high- z very challenging (e.g. Vito et al. 2018). All these observational issues can introduce relevant selection effects in all the estimates of the number of jetted AGNs at different cosmic epochs that are difficult to quantify.

A possible way out is to focus only on the sources that are seen at small angles from the jet direction, i.e. on blazars¹ (see e.g. Volonteri et al. 2011; Sbarro et al. 2015). Knowing that a blazar is typically observed at a viewing angle of $\theta \lesssim 1/\Gamma$, where Γ is the Lorentz factor of the bulk velocity in the jet, we can effectively use these objects to estimate the space density of all jetted AGNs in a region of Universe, with a purely geometrical argument. Specifically, the total number of jetted AGNs (N_{jet}) in a given volume of Universe is expected to be: $N_{\text{jet}} \approx 2\Gamma^2 N_{\text{blazar}}$ i.e. there are about 200 RL AGNs for each observed blazar, assuming a typical $\Gamma = 10$ (e.g. Ghisellini et al. 2014b). Another great advantage of this method is that the powerful jet is thought to wipe out the material along its path in the AGNs earlier stage, and hence obscuration effects are expected to be negligible. This makes the identification and the characterization of the optical counterpart more efficient and reliable. Therefore, from the estimate of the blazar space density it is possible to derive, in principle, a complete census of the entire jetted AGNs population without the biases due to radio emission anisotropy and to obscuration.

The application of this method requires the existence of flux-limited and statistically complete samples of blazars. In this paper we will use the *Cosmic Lens All Sky Survey* (CLASS, Myers et al. 2003; Browne et al. 2003) to build one of the largest radio flux limited samples of blazars covering a large fraction of the sky ($\sim 16300 \text{ deg}^2$) and that includes sources up to $z \sim 5.5$. In particular, we are interested in tracing the evolution of the most massive SMBHs ($\geq 10^9 M_\odot$) where a large difference in the evolutionary properties has been recently reported (e.g. Ajello et al. 2009; Ghisellini et al. 2010; Volonteri et al. 2011; Sbarro et al. 2015). Although for some objects in our sample the estimate of the SMBH masses is present in the literature (e.g. Shen et al. 2011) all the masses are recomputed here following a single coherent method. In this way our analysis should be free from possible biases that can derive from using different techniques (or emission lines) for sources located at different redshifts.

The paper is organized as follow. In Sect. 2 we describe the

¹ This category contains both sources with optical spectra characterized by strong emission lines (*Flat Spectrum Radio Quasars*, FSRQs) and sources with featureless optical spectra (BL Lac objects, Urry & Padovani 1995). Throughout this paper we will focus on the former species, therefore we will use *blazar* as a synonymous for FSRQ.

selection process of our luminosity-limited sample. In Sect. 3 we describe the analysis of the spectra and the estimation of the relevant parameters, furthermore we discuss the potential issues that could affect our estimates. In Sect. 4 we derive the number density of SMBHs with $M \geq 10^9 M_\odot$ hosted in blazars and in all the jetted AGNs. In Sects. 5 and 6 we discuss the results and we draw our conclusions. Throughout the paper we assume a flat Λ CDM cosmology with $H_0 = 70 \text{ km s}^{-1} \text{Mpc}^{-1}$, $\Omega_\lambda = 0.7$ and $\Omega_M = 0.3$.

2 THE SAMPLE

We start our selection from the CLASS, a radio survey at 5 GHz of flat-spectrum radio sources that covers most of the northern sky (16300 deg^2) and that contains ~ 11000 sources. This catalogue was built by combining the NRAO *Very Large Array Sky Survey* (NVSS), at 1.4 GHz (Condon et al. 1998), with the Green-Bank Survey (GB6) at 5 GHz (Gregory et al. 1996) and by selecting only the objects with a flat spectrum between 1.4 and 5 GHz ($\alpha < 0.5$, with $f_\nu \propto \nu^{-\alpha}$) with a final follow-up at 8.4 GHz using the *Very Large Array* (VLA) in the largest configuration (A), that granted an angular resolution of $\sim 0.2''$. The sub-arcsecond accuracy of the radio sources positions proved to be crucial to find the correct optical counterpart, in particular at faint magnitudes. Since blazars are flat-spectrum radio sources, CLASS represents the most efficient and reliable starting point to select a radio flux-limited sample of these sources suitable for statistical analyses.

We have recently carried out a specific search for blazars with redshift above 4 in the CLASS survey by efficiently pre-selecting candidates from the Pan-STARRS1, PS1, (Chambers et al. 2016), using the so-called drop-out technique (see Caccianiga et al. 2019 for details). Nearly all the candidates with a magnitude brighter than 21 (in the r , i or z filter, depending on the expected redshift of the source) have been spectroscopically confirmed, producing a list of 25 $z \geq 4$ AGNs. The spectroscopic data are gathered from the *Sloan Digital Sky Survey* (SDSS, Blanton et al. 2017; SDSS-I/II and the Baryon Oscillation Spectroscopic Survey, BOSS; $R=1500$ at $\lambda = 3800\text{\AA}$ and $R=2500$ at $\lambda = 9000\text{\AA}$) when available, or from dedicated observations using the *Multi-Object Double Spectrograph* (MODS) of the *Large Binocular Telescope* (LBT) with the red grating (G670L, 5000–10000 \AA ; $R=2300$ at $\lambda = 7600\text{\AA}$), or with the *Telescopio Nazionale Galileo* (TNG) coupled with the Device Optimized for the LOw RESolution (DOLORES, using the LR-R/LR-B grisms; respectively, $R=450$ at $\lambda = 4500\text{\AA}$ and $R=360$ at $\lambda = 7500\text{\AA}$), as detailed in Caccianiga et al. (2019). The analysis of the radio spectra (Caccianiga et al. 2019) and of the X-ray data (Ighina et al. 2019; Ighina et al. 2021) have then confirmed the blazar nature for 22 of these objects. If we restrict the search area to the high Galactic latitudes ($|b''| \geq 20 \text{ deg}$) where the identification level is close to 100%, 3 out of 22 blazars are excluded. The resulting 19 objects constitute the high- z complete sample, hereafter C19, with a sky coverage area of 13120 deg^2 .

To extend this sample at lower redshifts ($1 < z < 4$) we have considered the CLASS sources falling in the sky area covered by the SDSS Data Release 14 (DR14, Abolfathi et al. 2018) in order to benefit of the large spectroscopic database available for most of the brightest objects. Since we are interested in the most massive SMBHs, that are hosted in the most luminous AGNs, the SDSS spectroscopic data are deep enough to obtain a sample with a high spectroscopic identification level. We have thus cross-correlated CLASS with the SDSS DR14 photometric catalogue using a 1"

positional tolerance to guarantee that all the counterparts are recovered (see below). We have found a counterpart for about 74% of the CLASS sources in the SDSS area (6244 out of 8389). We have then verified that the large majority (95%) of these counterparts have a distance from the CLASS position less than 0.3'' thus confirming the high completeness of the radio/optical association. About 50% of the counterparts have a spectroscopic identification. This fraction, however, dramatically increases when considering the brightest sources, leading to a high identification level of the final sample, as explained below.

In order to select sources with the same radio and optical luminosities as in the C19, we can translate the radio and optical flux limits of the high-z sample of C19 ($m_{AB} \leq 21$ and $S_{5\text{GHz}} \geq 30 \text{ mJy}$) into luminosity lower limits at lower redshifts, assuming a starting redshift of $z=4$, namely:

$$\lambda L_\lambda(1350\text{\AA}) \gtrsim 10^{46} \text{ erg s}^{-1} \quad (1)$$

$$P_{5\text{GHz}} \gtrsim 10^{27} \text{ W Hz}^{-1} \quad (2)$$

We also decided to consider only sources with $z > 1.5$. The main reason for this choice is that the inclusion of lower redshift objects in the analysis would have required to consider an additional emission line for the SMBH estimate (i.e. H β , if CIV1549 \AA is not visible; see Section 3 for details). The use of multiple emission lines may introduce some systematic that can affect the final results. In any case, our goal is to better sample the redshift range between 2 and 4 where the blazar space density is expected to peak and, therefore, excluding sources below $z=1.5$ does not affect our analysis. We also exclude the objects with $z \geq 4$, that are already included in the C19 part of the sample.

As mentioned above, we want to analyse a FSRQ sample, hence we exclude BL Lac objects. Finally, we exclude the objects with low Galactic latitude ($|b''| < 20$), by analogy with the selection of C19. The resulting $1.5 < z < 4$ sub-sample contains 361 objects, with a sky coverage area $\sim 10700 \text{ deg}^2$.

We have then evaluated the completeness of this sample. As mentioned above, not all the CLASS sources in the SDSS area are spectroscopically identified in the literature. We worked out a correction to account for the missing sources.

As a first step, we split the sample in 8 bins of redshift. Then, we have translated the radio and optical flux limits of the high-z sample of C19, starting from redshift $z=4$, at lower redshifts, using the following relations:

$$\text{mag}_r(z) = 20.86 + 5 \log \left(\frac{D_L(z)}{D_L(4)} \right) + 2.5(\alpha_O - 1) \cdot \log \left(\frac{1+z}{1+4} \right) \quad (3)$$

$$S_{5\text{GHz}}(z) = 30 \left(\frac{D_L(4)}{D_L(z)} \right)^2 \left(\frac{1+4}{1+z} \right)^{(\alpha_R - 1)} \text{ mJy} \quad (4)$$

where $\text{mag}_r(z)$ is the Galactic-extinction corrected PS1 magnitude limit in the r -filter and $S_{5\text{GHz}}(z)$ is the radio flux density limit (at 5 GHz) at redshift z ; 20.86 is the magnitude limit used in the C19 sample (21th magnitude) corrected for the average Galactic Extinction of the C19 sample; $D_L(z)$ is the luminosity distance at redshift z ; α_O and α_R are the optical and radio spectral indices respectively. In particular, assuming $S(\nu) \propto \nu^{-\alpha}$ we use $\alpha_O = 0.44$ (Vanden Berk et al. 2001) and $\alpha_R = 0^2$. The Eqs. 3 and 4 are equivalent to Eqs. 1 and 2, and represent *de facto* a luminosity

² We estimate that the scatter of the optical index (~ 0.1) could result

selection.

We can therefore compute the radio and optical flux limits, using the value of redshift in the centre of each bin. We then compute the identification level for each bin, as the fraction of the CLASS sources above these limits in the SDSS sky area with a spectroscopic identification in the literature. The inverse of this number gives the multiplicative factor (C_{id}) to correct for the identification level. This correction range from 1.16 (at low redshifts) to 1.45, at redshift ~ 3.5 .

Moreover, some spectroscopically identified objects present in the literature lack a SDSS spectrum. For these objects we are not able to estimate the mass of the central BH. Nevertheless, under the assumption that all these blazars (either with spectrum or not) share the same properties, we can take into account the missing spectra with a second correction. Similarly to the C_{id} , we calculate this correction for each bin of redshift, specifically we compute the fraction of objects with a spectrum available from SDSS, and included in the CLASS, in each redshift bin and the correction is defined as the inverse of this number (hereafter, C_{spect}). The correction ranges from 1.02 to 1.15. In Tab 1 we report the values of C_{id} and C_{spect} for each redshift bin.

The uncertainties on these coefficients are evaluated assuming a binomial distribution $B(N, p)$, where N is the total number of sources in each bin of redshift for the considered correction, and p is the inverse of the true correction. Specifically, we are interested here in the compound uncertainty obtained by multiplying the two corrections. We evaluate, through a Monte Carlo simulation, that the impact of these statistical uncertainties on the final result are at most $\sim 6\%$.

Using these corrections we can obtain a reliable estimate of the actual number of blazars expected in each redshift bin. For the $z > 4$ sub-sample these correction are not necessary since the identification level is almost 100% (see C19 for details).

2.1 Confirming the blazar nature

By definition, the CLASS survey should only contain sources with a flat spectrum (i.e. blazars) between 1.4 and 5 GHz. However, since the spectral index estimate is based on two frequencies only, other AGNs with more complex radio spectra may be included in the CLASS. This is the case for Gigahertz Peaked Spectrum (GPS) sources, which are thought to be young and compact AGNs and that show a peak in the radio spectrum at high frequencies (1–5 GHz, O'Dea 1998). If the peak falls in the observed 1.4–5 GHz range, the corresponding source can be misinterpreted as a FSRQ. We expect that most of the sources with a GPS spectrum are not oriented sources, i.e. blazars³. In order to confirm the blazar nature of the CLASS sources, we considered their X-ray properties, which can be used as an independent and reliable proxy to assess the presence of relativistic beaming (e.g. Ghisellini 2015, Ighina et al. 2019). Indeed, an X-ray emission significantly higher than that expected from a RQ AGN with the same optical/UV luminosity is a robust evidence of the presence of an extra emission coming from an oriented relativistic jet.

in a $\sim 2\%$ scatter on the number of selected blazars, while the typical uncertainties on the radio spectral index in CLASS (~ 0.35) could cause a $\sim 9\%$ scatter.

³ This is not always true, however, as demonstrated by the existence of blazars showing a peaked radio spectrum like J0906+6930 at $z=5.47$ (Romani et al. 2004; Coppejans et al. 2017; An & Romani 2018; An et al. 2020)

z bin	S _{5GHz}	m _{AB}	C _{id}	C _{spect}
1.50 - 1.75	140	18.88	1.16	1.14
1.75 - 2.00	108	19.21	1.18	1.09
2.00 - 2.25	86	19.49	1.22	1.09
2.25 - 2.50	71	19.74	1.26	1.08
2.50 - 2.75	60	19.96	1.31	1.02
2.75 - 3.00	51	20.16	1.34	1.05
3.00 - 3.50	42	20.42	1.39	1.08
3.50 - 4.00	33	20.72	1.45	1.15

Table 1. Values of C_{id} and C_{spect} for different redshift bins (z<4 subsample). column 1: redshift interval; column 2 and 3: respectively, lower radio-flux (mJy) limit and lower magnitude limit calculated at the central redshift of each bin (see Eqs. 3, 4); column 4 and 5: Multiplicative factors that correct for the missing identification of the sample and for the lack of SDSS spectra, respectively.

To this end, we collected X-ray data from the second *Swift*-XRT point sources catalog (2SXPS, Evans et al. 2020). We found 107 detections (35% of the sample). After combining the X-ray fluxes with the optical properties from SDSS, we compute the $\tilde{\alpha}_{ox}$ ⁴ parameter for all these AGNs. We find that the large majority of these sources ($\sim 94 - 96\%$, depending on the assumption on the photon index, $\Gamma=1.5-1.8$) are strong X-ray emitters in the typical range observed in blazars ($\tilde{\alpha} < 1.355$, see e.g. Ighina et al. 2019). It should be noted that the ~ 100 CLASS sources detected in the 2SXPS catalog could not be representative of the entire sample. Indeed, the 2SXPS catalogue is based on archival pointed data and, therefore, blazars could be over-represented since they have been preferentially pointed by *Swift*-XRT. To avoid this possible bias, we also considered in the computation only the sources that are serendipitously detected by *Swift*-XRT, i.e. sources that were not specifically pointed. Using this sample, that contains 24 sources, we confirm a similar abundance of blazars (i.e. $\sim 92 - 96\%$). We note that these results are consistent with what found in the z>4 C19 sample, where about 90% of radio selected candidates were confirmed as blazars using the X-rays data (Ighina et al. 2019). We expect this fraction is representative of the whole sample, including the sources not yet observed in the X-rays, and, therefore, we apply a scale correction to the low-redshift (z<4) blazar density calculated in Section 4 to take into account the presence of this small fraction (6%) of non-blazars sources, in the sample.

3 ESTIMATING THE MASSES OF THE SMBHs

One of the most used and reliable method to calculate the mass of the central SMBH in type-I AGNs, is based on the virial theorem applied to the Broad Line Region (BLR). Assuming a completely virialized BLR we can compute the mass of the central BH from the BLR size and from the velocity dispersion of the orbiting clouds that form it:

$$M_{\text{BH}} = f \frac{R_{\text{BLR}} \Delta V^2}{G} \quad (5)$$

Where ΔV is a measure of the velocity dispersion of the BLR clouds, and R_{BLR} is a measure of the BLR size. f is a dimensionless factor that depends on the structure and the geometry of the BLR (e.g., Vestergaard & Peterson 2006, hereafter VP06).

The Doppler broadening of the line provides the necessary

information about the velocity dispersion of the ionized gas where the lines are produced. The BLR radius, instead, can be inferred from the continuum (or the line) luminosity using scaling relations of the form of $R \propto L^k$ (e.g., Kaspi et al. 2000; Grier et al. 2019). This relationship can therefore be used to estimate the radius of the BLR from a single luminosity measure, without the need of a continuous monitoring of the source. For this reason, this method is called *single epoch* (SE).

Among all the possible Broad Emission Lines (BELs), just a few of them are strong enough to be used for a reliable estimate of the BH mass: H β λ 4861, MgII λ 2799 and CIV λ 1549 are the most studied and used (e.g. Vestergaard & Peterson 2006; Shen & Liu 2012; Bentz 2015). With an AGN sample that covers a large range of redshift, the natural choice among the aforementioned three is the triply ionized carbon line (CIV λ 1549). Even though there are some concerns about the use of this line to estimate the SMBH masses (see Subsection 3.3 for a discussion of these potential issues), we decide to use this line since it is observable from $z \sim 1.5$ up to $z \sim 5.5$ in an optical spectrum and, therefore, it can be consistently used for the entire sample. This is a great advantage with respect of using different emission lines (or even different methods) depending on the redshift, something that can introduce unpredictable biases in the analysis of the space density versus z .

There are different ways to quantify the line width, the most common one being the Full Width at Half Maximum (FWHM). However, several authors (e.g. Vestergaard & Peterson 2006; Denney et al. 2013) suggest that the σ_l (line dispersion) can give more reliable results for the BH mass estimate. For instance, by comparing the CIV based masses with those derived with other independent methods, Denney et al. (2013) has concluded that the line dispersion can lead to BH masses with a lower scatter (<0.3 dex) if compared to FWHM, provided that high quality spectra ($S/N \gtrsim 10$) are used. We decide to compute the BH mass using both the line dispersion and the FWHM, to facilitate the comparison with the literature. In particular, we use the two relations derived by Vestergaard & Peterson (2006):

$$M_{\text{BH}}(\text{CIV}) = 10^{6.66} \left(\frac{\text{FWHM}(\text{CIV})}{10^3 \text{ km s}^{-1}} \right)^2 \left(\frac{\lambda L_\lambda(1350\text{\AA})}{10^{44} \text{ erg s}^{-1}} \right)^{0.53} \quad (6)$$

$$M_{\text{BH}}(\text{CIV}) = 10^{6.73} \left(\frac{\sigma_l(\text{CIV})}{10^3 \text{ km s}^{-1}} \right)^2 \left(\frac{\lambda L_\lambda(1350\text{\AA})}{10^{44} \text{ erg s}^{-1}} \right)^{0.53} \quad (7)$$

where the line dispersion and the FWHM are measured in km s^{-1} and $\lambda L_\lambda(1350\text{\AA})$ is the continuum luminosity at 1350\AA (source rest-frame) measured in erg s^{-1} . The intrinsic scatter of these relations is 0.3–0.4 dex (see Vestergaard & Peterson 2006) and it represents the main source of uncertainty in the mass estimate.

⁴ $\tilde{\alpha}_{ox} = -0.3026 \log(L_{10keV}/L_{2500})$ as in Ighina et al. (2019).

name	z	AV	r-mag	$S_{5\text{GHz}}$ (mJy)	σ_l (km s $^{-1}$)	FWHM (km s $^{-1}$)	$\log \lambda L_{1350}$ (erg s $^{-1}$)	$\log L_{CIV}$ (erg s $^{-1}$)	$\log L_{\text{bol}}$ (erg s $^{-1}$)	$\log M_\sigma$ (M_\odot)	$\log M_{\text{FWHM}}$ (M_\odot)	$\log \lambda_{\text{Edd}}$ [σ_l]	$\log \lambda_{\text{Edd}}$ [FWHM]
GB6J001115+144608	4.96	0.242	19.62	31	3310 ± 138	7548 ± 322	47.326 ± 0.004	45.240 ± 0.012	47.979 ± 0.004	9.53 ± 0.04	10.18 ± 0.04	0.35 ± 0.04	-0.30 ± 0.04
GB6J012202+030951	4.00	0.161	20.86	96	-	5800 ± 2000	46.450 ± 0.070	-	47.103 ± 0.070	-	9.52 ± 0.39	-	-0.51 ± 0.39
GB6J083548+182519	4.41	0.141	21.18	40	2191 ± 89	5032 ± 211	46.104 ± 0.029	44.497 ± 0.016	46.757 ± 0.029	8.53 ± 0.04	9.18 ± 0.04	0.13 ± 0.04	-0.52 ± 0.04
GB6J083945+511206	4.40	0.175	19.37	51	5463 ± 119	5806 ± 280	46.795 ± 0.005	45.103 ± 0.007	47.448 ± 0.005	9.69 ± 0.02	9.67 ± 0.04	-0.34 ± 0.02	-0.32 ± 0.04
GB6J090631+693027	5.47	0.204	20.54	100	-	-	-	-	-	9.30 ± 0.39	9.30 ± 0.39	-	-
GB6J091825+063722	4.22	0.163	19.86	36	3031 ± 109	6967 ± 266	46.702 ± 0.009	44.782 ± 0.014	47.355 ± 0.009	9.13 ± 0.03	9.78 ± 0.03	0.13 ± 0.03	-0.52 ± 0.03
GB6J102107+220904	4.26	0.095	21.21	108	3751 ± 357	3097 ± 325	46.007 ± 0.026	44.562 ± 0.015	46.660 ± 0.026	8.94 ± 0.08	8.71 ± 0.10	-0.38 ± 0.08	-0.15 ± 0.09
GB6J102623+254255	5.28	0.079	21.95	142	4183 ± 488	5613 ± 510	46.692 ± 0.011	45.144 ± 0.022	47.345 ± 0.011	9.40 ± 0.10	9.58 ± 0.08	-0.16 ± 0.10	-0.34 ± 0.08
GB6J132512+112338	4.42	0.105	19.41	62	3463 ± 82	3484 ± 356	46.568 ± 0.008	45.208 ± 0.011	47.221 ± 0.008	9.17 ± 0.02	9.10 ± 0.10	-0.05 ± 0.02	0.02 ± 0.10
GB6J134811+193520	4.40	0.098	20.73	38	5359 ± 280	4838 ± 247	46.337 ± 0.013	44.609 ± 0.012	46.990 ± 0.013	9.43 ± 0.05	9.27 ± 0.05	-0.54 ± 0.05	-0.38 ± 0.04
GB6J141212+062408	4.47	0.110	20.23	34	3052 ± 313	7161 ± 749	46.494 ± 0.015	44.252 ± 0.020	47.147 ± 0.015	9.02 ± 0.08	9.69 ± 0.09	0.03 ± 0.08	-0.65 ± 0.09
GB6J143023+420450	4.71	0.058	21.00	337	3541 ± 186	8129 ± 450	46.627 ± 0.011	44.602 ± 0.014	47.280 ± 0.011	9.22 ± 0.05	9.87 ± 0.05	-0.04 ± 0.05	-0.69 ± 0.05
GB6J151002+570256	4.31	0.078	20.34	292	2540 ± 113	2322 ± 272	46.532 ± 0.010	44.830 ± 0.014	47.185 ± 0.010	8.88 ± 0.04	8.73 ± 0.11	0.20 ± 0.04	0.35 ± 0.11
GB6J153533+025419	4.39	0.213	20.59	53	3461 ± 219	7935 ± 528	46.363 ± 0.013	44.363 ± 0.017	47.016 ± 0.013	9.06 ± 0.05	9.71 ± 0.06	-0.15 ± 0.06	-0.80 ± 0.06
GB6J162956+095959	5.00	0.283	21.97	33	2436 ± 779	5613 ± 1819	46.314 ± 0.151	44.079 ± 0.114	46.967 ± 0.151	8.73 ± 0.32	9.38 ± 0.33	0.14 ± 0.32	-0.52 ± 0.32
GB6J164856+460341	5.36	0.000	20.31	36	2604 ± 207	4645 ± 2100	46.260 ± 0.142	44.601 ± 0.045	46.913 ± 0.142	8.76 ± 0.11	9.19 ± 0.73	0.05 ± 0.10	-0.38 ± 0.71
GB6J171103+383016	4.00	0.221	20.52	36	2188 ± 126	2129 ± 216	46.280 ± 0.015	44.542 ± 0.014	46.933 ± 0.015	8.62 ± 0.05	8.52 ± 0.10	0.21 ± 0.05	0.31 ± 0.10
GB6J231449+020146	4.11	0.267	19.59	84	3975 ± 395	2903 ± 267	46.307 ± 0.010	45.164 ± 0.013	46.960 ± 0.010	9.15 ± 0.08	8.81 ± 0.09	-0.29 ± 0.08	0.05 ± 0.09
GB6J235758+140205	4.35	0.191	20.43	78	3182 ± 124	7161 ± 305	46.267 ± 0.015	44.327 ± 0.017	46.920 ± 0.015	8.94 ± 0.04	9.57 ± 0.04	-0.12 ± 0.03	-0.75 ± 0.04

Table 2. Properties of the high-redshift blazars (C19). **column 1:** source name; **column 2:** redshift; **column 3:** total extinction in the V-band; **column 4:** magnitude in the r-filter ; **column 5:** radio flux density measured at 5GHz; **columns 6 and 7:** CIV line dispersion and FWHM; **column 8:** continuum luminosity at 1350Å **column 9:** CIVλ1549 line luminosity; **column 10:** bolometric luminosity, calculated assuming a bolometric correction $K_{\text{bol}}(1350\text{\AA}) = 4.5$; **columns 11 and 12:** SMBH mass, estimated using the VP06 relations (see text); **columns 13 and 14:** Eddington ratios calculated using the masses derived from the line dispersion and the FWHM, respectively. The parameters of GB6J012202+030951 are inferred from the printed spectrum, whereas the mass of GB6J090631+693027 has been calculated in Romani (2006). In this table we report statistical uncertainties only. Please note that the calibration uncertainties in the VP06 are indeed the main source of scatter (0.3–0.4 dex, see text) in the mass estimate.

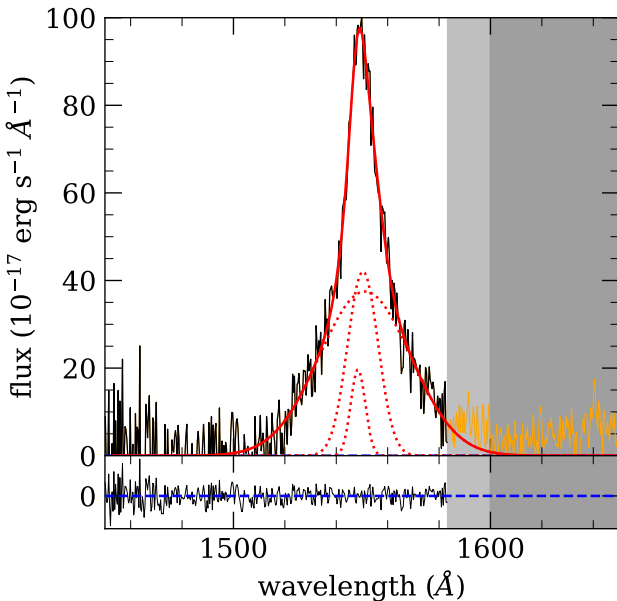


Figure 1. Example of the fitting procedure (GB6J162030+490149). The top panel represents the rest-frame continuum-subtracted spectrum. The mask applied is represented with the grey shaded area and in orange is shown the excluded part of the spectrum. The best-fitting model for the CIV line is represented with the solid red line, while the single gaussian components are depicted with the dotted red line. The bottom panel shows the residuals.

3.1 Spectral analysis

The procedure used to isolate and analyze the CIV emission line follows that described in Denney et al. (2016). The observed spectra are firstly corrected for Galactic extinction (Fitzpatrick 1999). The redshift of the source is spectroscopically determined. We then bring the spectrum to the source rest-frame and linearly fit the continuum around the CIV emission line, using default windows of 1435–1465Å and 1690–1710Å (Denney et al. 2016). When the data within these boundaries are affected by spurious features or fall at the edge of the spectrum, other intervals are manually selected to estimate the continuum around the emission line. In many cases it was necessary to mask one or more regions containing spurious features, such as the emission often observed between CIV and HeIIλ1640 (which requires a default mask between 1600Å and 1680Å, as in Denney et al. 2016), telluric absorptions, sky line residuals and cosmic rays. The fitting of the CIV line is performed with a multi-gaussians model (1, 2 or 3 depending on the spectrum and the data quality). To better illustrate the method, we report in Fig. 1 an example of the spectra preparation.

The fit parameters uncertainties are calculated using a Monte Carlo approach. For each object we create N independent spectra based on the observed spectrum with a gaussian-distributed noise added. The noise is derived from the *inverse variance* vector when available, or from the RMS calculated in the continuum-subtracted spectrum around the line, when the vector was not present. For each mock spectrum the parameters are then estimated. After one thousand iterations, the standard deviation for each parameter is calculated and assumed as its uncertainty.

The best-fitting parameters with their uncertainties are reported in

Table 2⁵. In particular, we show the best-fitting parameters of the $z>4$ sources while the values for the entire sample are reported in the Appendix.

3.2 Eddington Ratio

Another important parameter related to the mass of the central BH is the Eddington ratio i.e. the ratio between the bolometric luminosity and the Eddington luminosity:

$$\lambda_{edd} = L_{bol}/L_{Edd} \quad (8)$$

where $L_{Edd} = 1.26 \cdot 10^{38} M/M_\odot$ erg s⁻¹ and the bolometric luminosity is the total energy produced by the AGN per unit of time integrated on all the wavelengths. This parameter can be estimated using a bolometric correction (K_{bol}) that allows the calculation of the bolometric luminosity starting from a monochromatic luminosity at a given wavelength ($L_{bol}=K_{bol} \cdot \lambda L_\lambda$). Here, we use an average K_{bol} derived from Shen et al. (2020): $K_{bol}(1450\text{\AA})=4.68$, which can be translated at 1350Å using the average spectral index, resulting in $K_{bol}(1350\text{\AA}) \approx 4.5$. The resulting values of Eddington ratios of the $z>4$ objects are reported in Table 2 while those of the entire sample appear in the Appendix.

3.3 Potential issues

Besides the statistical errors and the intrinsic scatter of the VP06 relations, the masses derived via the SE method are potentially affected by some (possible) systematics. We briefly discuss here the most important ones trying to establish their actual relevance on the sample considered in this work. At the end of the section we will present an independent measure of the masses showing that these biases, if present, should have a modest impact on our results (also considering the large statistical uncertainties). The main potential biases that may affect our SE-derived masses are:

- **Orientation - Blazars** are face-on RL AGNs. This means that we are likely observing these objects within $\sim 10^\circ$ from the jet direction (e.g. Savolainen et al. 2010; Ajello et al. 2012). It has been suggested (e.g. Decarli et al. 2008, 2010) that the typical BLR may have a disc-like structure and that the observed line widths are therefore significantly dependent on the particular orientation of the source since we only measure the projected component of the dispersion velocity. Therefore, in a nearly face-on source, the line width could be significantly lower than the edge-on case even if the mass of the central SMBH is the same. For a sample of randomly distributed AGNs, this effect will increase the scatter of the derived masses. In a sample of AGNs with a specific orientation, like blazars, the masses could be systematically biased. The SE relations (Eqs 6 and 7) are calibrated on several low-redshift quasars, for which we expect a random orientation (from 0 to ~ 45 degrees, by definition of type-I AGN). The SE relations are therefore strictly correct for a mean spatial angle, probably close to $\sim 30^\circ$. For sources observed at lower/larger angles, the derived mass is expected to be under/over estimated, respectively. However it is not clear if all the BELs are affected by orientation. This kind of bias has been actually measured by Runnoe et al.

⁵ Two objects at $z>4$, i.e. GB6J012202+030951 and GB6J090631+693027, lack a SDSS spectrum, therefore for the former objects we infer the parameters from the printed spectra, whereas the properties of the latter object are taken from the literature (Romani 2006).

(2014) for masses calculated using H β but it has not been found for CIV-based masses. A similar result has been achieved by Fine et al. (2011) using a sample of RL AGNs, finding no significant correlation between the CIV line width and the BLR orientation. The proposed explanation is that the highly ionized CIV line is probably produced in a different (more isotropic) region of the BLR. Therefore, we expect that the viewing angle is not a relevant issue in our estimate. However, as discussed in the next section (see 3.4), we have assessed this possible systematic using a completely independent method.

- **Jet contamination and disk anisotropies** - These potential issues are connected, again, with the orientation. Firstly, the luminosity of a relativistic jet observed at small angles is significantly amplified by the relativistic beaming (Urry & Padovani 1995). In principle, this emission could contaminate the continuum emitted by the accretion disk. Therefore, a continuum-luminosity based relationship, like the one we are using (Eqs. 6 and 7), may lead to a mass overestimate (e.g. Decarli et al. 2010). Secondly, the continuum luminosity is known to be produced by a geometrically thin and optically thick disc-like structure, which means that the observed luminosity is higher when viewed face-on (Calderone et al. 2013). This effect could also lead to overestimate the mass, since the SE relations are calibrated on the average orientation of type-I AGNs, while we are applying them to sources observed face-on. In order to evaluate the impact of these potential bias on the SE masses, we have compared the CIV line luminosities (which are not affected by disc-inclination effects) against the continuum luminosities at 1350Å (which could be affected by the beaming). We then compared this relation with a similar one derived by Shen & Liu (2012) from a large sample of radio-quiet AGNs for which the beaming is not present and that are expected to be observed, on average, at larger angles compared to blazars. If the viewing angle plays a significant role in the observed continuum luminosity, we should observe a systematic shift of this relation with respect to the one by Shen & Liu (2012). Nevertheless, comparing the luminosities of the objects in our sample with those estimated in Shen et al. (2011) we find no evidence of a significant contamination (see Fig. 2). In particular, we can quantify the possible offset by considering the ratio $R = \log(L_{1350}/L_{CIV})$ in both the randomly aligned sample and in our sample. The two values ($R_{\text{Shen}} = 1.62 \pm 0.28$ and $R_{\text{blazar}} = 1.61 \pm 0.25$) are fully consistent.

- **Issues on the CIV line as a virial indicator** - The SE method is based on the assumption that the line width arises from virial motions. However, as mentioned above, CIV BELs are affected by a blueshift, although this effect seems to be less relevant in RL AGNs (Richards et al. 2011). Due to the high ionization energy, CIV $\lambda 1549$ is likely to be produced in the innermost part of the BLR, as confirmed by reverberation mapping observations of the CIV time-lag (Sun et al. 2018), and this effect may imply the presence of a non virialized component of the BLR. Indeed, the radiation pressure from the accretion disc may affect the regular trajectory of the gas, with a net radial radiation flow that modifies the emission line profiles (Murray & Chiang 1997; Leighly 2004; Denney 2012). There have been many efforts to improve SE mass estimates from CIV (Denney 2012; Runnoe et al. 2014; Mejía-Restrepo et al. 2016; Coatman et al. 2016). Nevertheless, Denney et al. (2013) found that the second moment of the line (σ_l) is only marginally affected by blueshift and that the masses derived through this quantity are less scattered with respect to the masses derived from H β (provided that

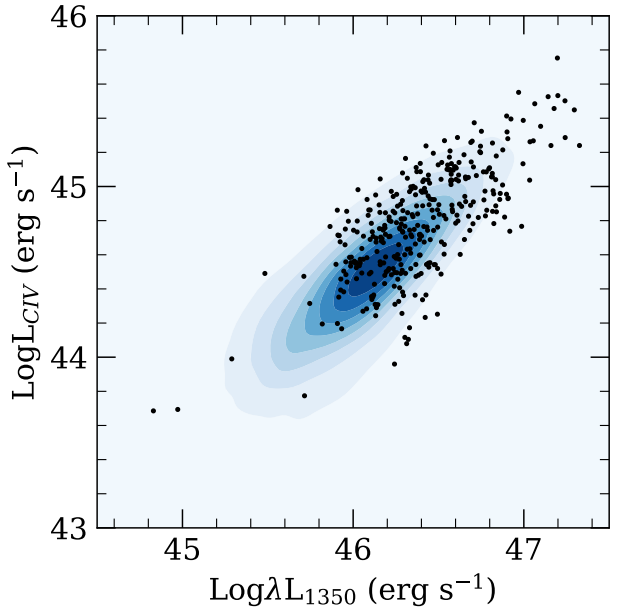


Figure 2. Continuum luminosity versus CIV line luminosity. The plot represents the relation between the continuum luminosities estimated at 1350Å and the integrated line luminosities of the CIV, in our sample (black dots). As reference, we use the luminosities estimated in Shen et al. (2011) using a sample of randomly oriented AGNs (represented here with the blue confidence regions, in 10% increments). There is no evidence of any contamination from the jet, which would result in a systematic offset of the points with respect to the Shen et al. (2011) sample.

the S/N of the spectrum is high enough, namely $S/N \gtrsim 10$ around 1450Å). For this reason, we decided to use the σ_l to quantify the line widths of our sample. To allow a direct comparison with the literature, however, we also compute and report in Table 2 and in the Appendix the values of masses obtained using the (more common) relations based on the FWHM.

3.4 Testing the SE masses

Even if the potential issues described in the previous sections are not expected to have a significant impact on our analysis, we decided to verify the presence of any possible bias on the calculated masses. To this end, we use an independent technique based on the accretion disc emission (e.g. see Calderone et al. 2013 for a detailed description of the method). This technique assumes that the optical/UV continuum emission of the AGN is produced by an optically thick, geometrically thin accretion disc (AD) that emits according to the Shakura & Sunyaev (1973, SS73) model. With these assumptions it is possible to derive the values of M_{BH} and of the accretion rate, that are free parameters of the SS73 model, simply by fitting the optical/UV data points. In spite of its simplicity, the AD method is not routinely used to derive the SMBH masses since it requires a good data coverage, in particular around the critical region where the disc emission peaks (i.e. the rest-frame UV region). For this reason, this method is typically applied to high-z objects ($z > 3-4$) for which the rest-frame UV region of the spectrum is relatively well sampled by the photometric points in the visible range. However, even in high-z sources the application of this technique could be problematic since the peak of the disc emission may fall at wavelengths bluer than

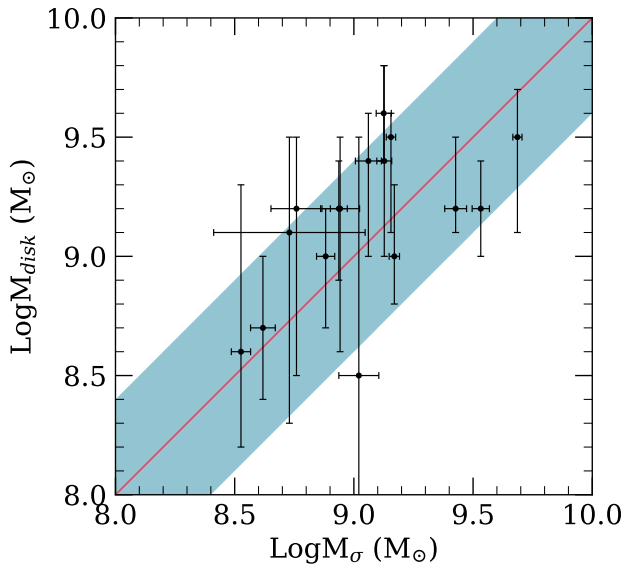


Figure 3. Comparison of the SMBH masses ($z \geq 4$) derived using the SE and the AD method. The red solid line is the 1:1 relation; in cyan, the region corresponding to the maximum intrinsic scatter of the VP06 relations (0.4 dex). No evident bias in the mass estimate can be revealed using this independent method.

the Ly $\alpha\lambda 1215$ where the effect of the neutral hydrogen absorption is very important, making the photometric points not usable. This happens, in particular, in sources hosting the least massive SMBHs ($< 10^8 M_\odot$).

With the main goal of testing the SE masses, we decided to apply the AD method to the high- z ($z \geq 4$) objects in the CLASS sample, for which the UV spectral range is relatively well sampled. The typical photometric coverage available for CLASS high- z sources is limited to the few data points from PS1 not affected by the neutral hydrogen absorption and to the observed spectrum. MID-IR points from the Wide-field Infrared Survey Explorer (WISE, Wright et al. 2010) cannot be used as they may be contaminated by the jet emission.

As a consequence of this limited data set, the resulting masses are poorly constrained, with typical uncertainties of ~ 0.3 – 0.6 dex, that are significantly larger than the statistical error on the masses derived from SE method (~ 0.05 dex) and comparable or even larger than the intrinsic error related to the SE method (~ 0.4 dex). In spite of these large uncertainties, the AD method can be still used to search for possible systematics in the SE masses. In Fig 3 we show the comparison between the SE masses of the C19 sample (based on Eq. 7) and the AD masses.

Given the large uncertainties of the AD masses, the two values are overall in good agreement ($\text{Log}(M_{\text{disk}}/M_{\text{SE}}) = 0.1 \pm 0.3$).

In conclusion, the masses derived with the SE method, although very uncertain, do not reveal systematic discrepancies when compared to the AD masses. This confirms that the potential biases, discussed in the previous section, if present, do not affect significantly the final results. We therefore consider the SE masses as our best estimates and we use them in the rest of the paper.

	Starting sample	With spectra	$M_{\text{SMBH}} \geq 10^9 M_\odot$
N sources	380	352	243

Table 3. Number of sources selected. The number of sources, between $z=1.5$ and $z=5.5$, in the progressively stringent sets considered. Respectively, the starting sample (Eqs. 1, 2 and $|b''| \geq 20$) composed by 361 objects with $1.5 \leq z < 4$ plus the C19 sample (19 sources with $4 \leq z < 5.5$); the objects with an available spectrum; the objects with a $M_{\text{SMBH}} \geq 10^9 M_\odot$ (considering the line dispersion relation, Eq. 7).

4 SPACE DENSITY EVOLUTION OF $\geq 10^9 M_\odot$ SMBHS HOSTED BY RL AGNS

An important test to assess the role of the relativistic jets in the evolution of the SMBHs across cosmic time is to compare the relative abundance of RL AGNs with respect to the total AGN population at different redshifts. The RL fraction in the local Universe has been the subject of several publications in the last years. The commonly accepted value was assessed to be about $\sim 10\%$ (e.g. Fanti et al. 1977; Condon et al. 1980; Smith & Wright 1980; Sramek & Weedman 1980; Hooper et al. 1995; Ivezić et al. 2002; Volonteri et al. 2011) although some more recent works have found that the RL fraction could be as high as 20–30% (e.g. Kellermann et al. 1989; della Ceca et al. 1994; Best et al. 2005; Jiang et al. 2007; Kellermann et al. 2016).

However, estimating this ratio at larger redshift is not as straightforward (e.g. Stern et al. 2000; Bañados et al. 2015; Yang et al. 2016; Liu et al. 2021). As already discussed, part of the radio emission, i.e. the one produced by the jet, is highly anisotropic because of the relativistic beaming that strongly boosts the emission along the jet direction. This problem is particularly important at high redshifts where we typically observe the high frequency (rest-frame) emission which is usually dominated by the jet while the isotropic component (from the radio lobes) is severely attenuated due to the steepness of the spectrum. In addition, the extended emission is more difficult to detect compared to the point-like core, especially with fluxes close to the survey sensitivities. Finally, the extended emission of RL AGNs is also expected to be significantly damped at high redshift due to the increased density of the CMB photons that interact and cool the relativistic electrons in the radio lobes (see e.g. Ghisellini et al. 2014a). All these potential issues make it difficult to assess whether the optically selected high- z AGNs currently not detected in the radio band are truly radio-quiet sources or simply misaligned jetted AGNs. Using blazars to trace the RL AGNs population, instead, we are not directly affected by these problems and, therefore, we can provide a reliable estimate of the true fraction of RL AGNs at all redshifts.

As discussed in Section 2, our sample is complete for radio powers larger than $P_{5\text{GHz}} \gtrsim 10^{27} \text{ W Hz}^{-1}$. Considering that we expect the radio luminosity in blazars to be boosted by 2 or 3 orders of magnitude⁶, this means that we are able to sample the population of RL AGNs down to an intrinsic radio power of $P_{5\text{GHz}} \sim 10^{24}$ – $10^{25} \text{ W Hz}^{-1}$ which is close to the typical threshold that divides radio-loud from radio-quiet AGNs (e.g. Kellermann et al. 2016; Padovani 2017). Considering the *deboosted* radio flux, our sample is sensitive to an intrinsic radio-loudness⁷. This means that we

⁶ The relativistic Doppler beaming can be expressed as $\delta^{n+\alpha}$, with a Doppler factor $\delta=1/(\Gamma(1-\beta\cos\theta))$, α is the radio spectral index, which in our case is $\alpha_R = 0$, and n ranges from 2 to 3 (see e.g. Singal 2016). Therefore, assuming $\sin\theta = 1/\Gamma$, we obtain a boost of $\Gamma^n = 10^2$ – 10^3 .

⁷ Defined as $R = f_\nu(5\text{GHz})/f_\nu(4400\text{\AA})$ rest-frame (Kellermann et al.

should be sensitive to the bulk of the RL AGNs population up to $z \sim 5.5$.

In principle, the presence of an optical limit (mag=21 for the $z \geq 4$ sample) may prevent the selection of the least (optical) luminous sources ($\lambda L_{\lambda}(1350\text{\AA}) < 10^{46}\text{erg s}^{-1}$). As previously discussed, however, we are focusing on the objects hosting the largest SMBH masses ($M \geq 10^9 M_{\odot}$, i.e. 243 sources, see Tab. 3). The limit on the optical luminosity can be translated into a limit on the bolometric luminosity:

$$L_{\text{bol}} = K_{\text{bol}}(1350\text{\AA}) \cdot \nu L_{\nu}(1350\text{\AA}) \simeq 5 \cdot 10^{46} \text{ erg s}^{-1} \quad (9)$$

For SMBH masses between 10^9 and $10^{10} M_{\odot}$, this limit implies that we are sensitive down to Eddington ratios of ~ 0.1 – 0.2 , i.e. again, to the bulk of the population of AGNs with quasar-like spectra (Shen et al. 2011). In summary, with the CLASS blazars we are able to evaluate the true space density of RL AGNs hosting the most massive SMBHs ($M \geq 10^9 M_{\odot}$) in the 1.5–5.5 redshift range.

First, for each source we calculate the comoving volume within which it could have been observed:

$$V_{\text{eff}} = \frac{A}{4\pi} V \quad (10)$$

where A is the sky coverage area in steradians of the two subsamples, i.e. 1.272π (or 13120 deg^2) above $z=4$, 1.038π (or 10700 deg^2) under $z=4$. V is the comoving volume between z_1 and z_2 . Please note that in this case it is not necessary to apply the method suggested in Avni & Bahcall (1980), since in our luminosity-limited sample each object is always detectable up to $z \sim 5.5$. The blazar space density in each bin (z_1, z_2) is therefore calculated as:

$$n_{\text{blazar}} = \frac{C_{\text{spect}} \cdot C_{\text{id}} \cdot N}{V_{\text{eff}}} \quad (11)$$

The sources of uncertainty in the blazars space density calculation are the coefficients (C_{id} and C_{spect} , distributed with a binomial pdf, see Section 2) and the Poisson uncertainty on the number of objects above the considered mass threshold ($M \geq 10^9 M_{\odot}$) which, in turns, depends on the uncertainty on the SE masses (Gauss distribution with standard deviation $\sigma = 0.3 M_{\odot}$, see Section 3). In order to evaluate the impact of these sources of uncertainties we performed a Monte Carlo simulation with 10^5 iterations.

Finally, we can consider the blazars space density inferred from the only $z \sim 6$ blazar known to date ($0.0055^{+0.0125}_{-0.0046} \text{ Gpc}^{-3}$, Belladitta et al. 2020 and Belladitta et al. submitted).

In order to evaluate the space density of all RL AGNs hosting a SMBH with $M_{\text{BH}} \geq 10^9 M_{\odot}$ (n_{jet}), as mentioned in Sec. 1, we use a simple geometrical argument:

$$n_{\text{jet}} = 2\Gamma^2 n_{\text{blazar}} \quad (12)$$

In this paper we assume a mean $\Gamma = 10$, therefore 1 blazar every ~ 200 RLs. The results are reported in Tab. 4 and in Fig. 4.

5 DISCUSSION

So far we have derived the space density of blazars hosting the most massive SMBHs ($\geq 10^9 M_{\odot}$) at $1.5 \leq z \leq 5.5$. Using a geometrical argument, assuming a viewing angle $\theta \sim 1/\Gamma$ and a typical Lorentz bulk factor $\Gamma = 10$, we have inferred the space density of all the jetted AGNs powered by the most massive SMBHs, in the considered

1989) above ≥ 10 , which is, again, the traditional dividing value between RL and RQ AGNs (Kellermann et al. 1989)

z bin	N _{bl}	Logn _{bl}	Logn _{jet}		
			Γ		
			5	10	15
1.50 – 1.75	26	$0.04^{+0.10}_{-0.11}$	1.74	2.34	2.69
1.75 – 2.00	26	$0.00^{+0.10}_{-0.11}$	1.70	2.31	2.66
2.00 – 2.25	37	$0.16^{+0.08}_{-0.09}$	1.86	2.46	2.82
2.25 – 2.50	30	$0.08^{+0.09}_{-0.09}$	1.78	2.38	2.73
2.50 – 2.75	34	$0.12^{+0.08}_{-0.09}$	1.82	2.42	2.78
2.75 – 3.00	31	$0.11^{+0.08}_{-0.09}$	1.81	2.41	2.76
3.00 – 3.50	33	$-0.12^{+0.08}_{-0.09}$	1.57	2.18	2.53
3.50 – 4.00	14	$-0.43^{+0.12}_{-0.13}$	1.27	1.87	2.22
4.00 – 4.50	8	$-0.94^{+0.15}_{-0.24}$	0.76	1.36	1.72
4.50 – 5.00	2	$-1.52^{+0.37}_{-0.45}$	0.18	0.78	1.14
5.00 – 5.50	2	$-1.49^{+0.37}_{-0.45}$	0.21	0.81	1.16

Table 4. Space density of the most massive ($\geq 10^9 M_{\odot}$) blazars in our sample. Column 1: redshift interval; column 2: the number of blazars, within the sample, with a mass $M \geq 10^9 M_{\odot}$ in each bin of redshifts in the covered sky area; column 3: logarithmic space density of blazars with $M \geq 10^9 M_{\odot}$ (measured in Gpc^{-3}); column 4, 5 and 6: logarithmic space density of jetted AGNs, inferred assuming three representative Lorentz bulk factors, i.e. $\Gamma = [5, 10, 15]$ (measured in Gpc^{-3}). The statistical uncertainties on the logarithmic jetted AGNs densities are the same as for the logarithmic blazar densities.

redshift interval. We want to stress that this estimate is by definition unaffected by the torus dust extinction, therefore we are including in our result both the type-I and the type-II AGNs, at least in the case that the obscuration is only due to a molecular torus. It is known that jetted AGNs represent a minority of the total population, and several works have tried to estimate the relative abundance of these objects. These estimates converge to 10–30% in the local Universe (e.g. Fanti et al. 1977; Condon et al. 1980; Smith & Wright 1980; Sramek & Weedman 1980; Hooper et al. 1995; Ivezić et al. 2002; Kellermann et al. 1989; Best et al. 2005; Jiang et al. 2007; Volonteri et al. 2011; Kellermann et al. 2016). However, it is still unclear if the jetted fraction have changed with cosmic time, especially at high-z, due to the lack of consistency in the samples at different redshifts and the intrinsic difficulty of observing partially or completely obscured jetted AGNs.

In order to compare the most massive SMBHs hosted in jetted AGNs with those hosted by the total AGN population, we would need complete samples containing the values of SMBH masses for each source, as in our sample of blazars. Alternatively, it is possible to use the *quasar luminosity function* (QLF) and integrate it above a certain *effective* luminosity, considering that SMBH mass and bolometric luminosity are tightly related⁸. In particular, we use the most recent QLF derived in Shen et al. (2020)⁹. This QLF is corrected for intrinsic absorption assuming the neutral hydrogen column distribution suggested in Ueda et al. (2014), and a redshift-dependent dust-to-gas ratio (Ma et al. 2015). Therefore, without further corrections, we can directly compare our results with this QLF.

In particular we integrate the QLF with a minimum luminosity:

$$n_{\text{AGN}}(z) = \int_{L_{\text{min}}^{\text{eff}}}^{\infty} n_{\text{AGN}}(z, L) dL \quad (13)$$

⁸ This is a reasonable assumption, at least in our sample, since M_{BH} and λL_{1350} are closely coupled.

⁹ There are proposed two different fit models (referred as *Global Fit A* and *B*), they only differ in dealing with the QLF faint-end slope. Here, we choose the model *Global Fit B*.

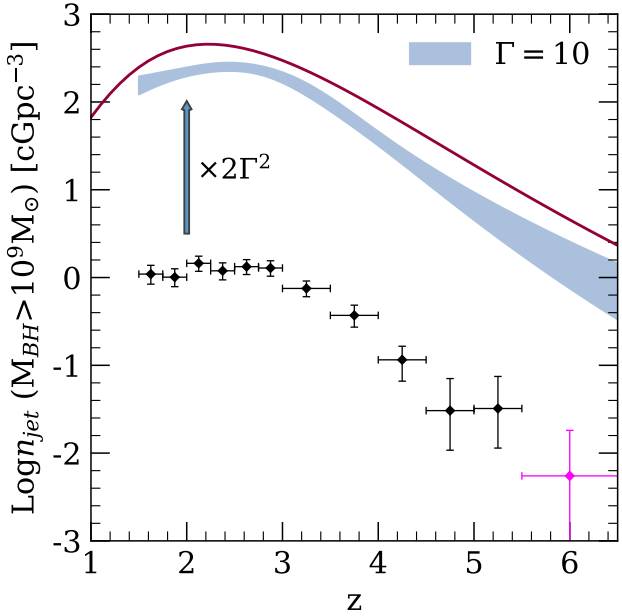


Figure 4. Comoving space density of different types of AGNs hosting black holes with $M \geq 10^9 M_\odot$ as a function of redshift. The black dots represent the space density of SMBHs with $M \geq 10^9 M_\odot$ hosted by FSRQs, estimated in this work. The magenta dot represents the blazars space density inferred from the only blazar known at $z > 6$ (Belladitta et al. 2020), which is in good agreement with the extrapolation of our points. The uncertainties on the densities are estimated using a Monte Carlo simulation (see text). The blue band indicates the space density of all RL AGNs, independently of orientation (i.e. including absorbed sources), as estimated from the blazar population. It is derived by fitting the black points and then scaling up the normalization by a factor $2\Gamma^2$, assuming a mean Lorentz factor $\Gamma = 10$. The delimited area represents 1σ confidence intervals, calculated using a Monte Carlo method. The dark red solid line is derived from the most recent QLF (Shen et al. 2020) which estimates the space density of both jetted and non-jetted AGNs, up to $z=6.5$. In particular, the QLF is integrated with $L_{\min}^{\text{eff}} \geq 8.4 \cdot 10^{46} \text{ erg s}^{-1}$, in order to represent only quasars similar to the bulk of our sample (see text).

Where $n_{\text{AGN}}(z)$ is the number density of AGNs hosting the most massive BHs ($\geq 10^9 M_\odot$); considering the objects with $M \geq 10^9 M_\odot$ in our sample, we can define L_{\min}^{eff} as the minimum luminosity to obtain the same number of objects within our full sample of 380 objects, regardless of M_{BH} , with $L_{\text{bol}} \geq L_{\min}^{\text{eff}}$. We find $L_{\min}^{\text{eff}} = 8.4 \cdot 10^{46} \text{ erg s}^{-1}$. Thus, we can integrate the QLF without assuming a specific Eddington ratio distribution.

The integrated QLF shows a luminosity dependent evolution, with a maximum density occurring at $z=2.2$ using the aforementioned lower luminosity (see Fig. 4, dark red line).

The first fact that emerges from the comparison is that the space density evolution of jetted AGNs here calculated is qualitatively similar to that observed in the total AGN population. This is in contrast with previous results that found a much more rapid evolution in X-ray selected blazars with similar masses, culminating at $z \sim 4$ (Ajello et al. 2009). One possible explanation for this discrepancy is that the X-ray-to-radio luminosity ratio of the jet emission strongly increases with redshift, as actually observed by several authors (e.g. Zhu et al. 2019 and Ighina et al. 2019). This increase is naturally expected if we consider the Inverse Compton interaction between the photons from the Cosmic Microwave Background (CMB) and the

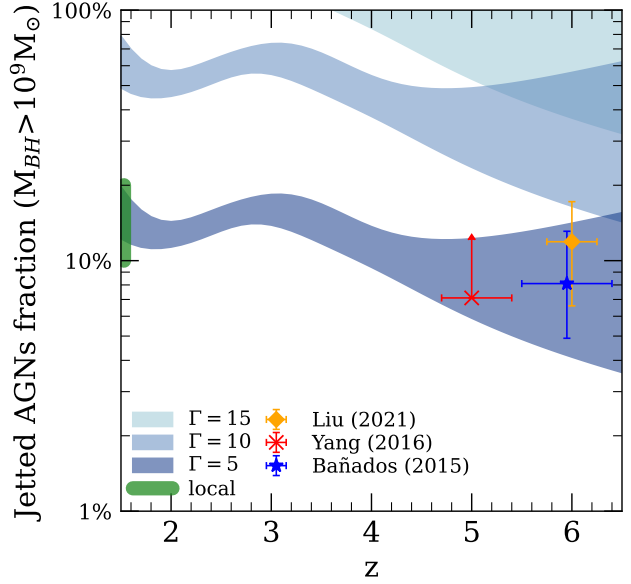


Figure 5. Fraction of jetted AGNs hosting the most massive SMBHs ($\geq 10^9 M_\odot$) as a function of redshift. We report here three different estimates assuming three values of the Lorentz factor: $\Gamma = [5, 10, 15]$. The uncertainties are estimated using a Monte Carlo method and are the same as in Fig. 4. Coloured dots represent previous estimates found in the literature (see the inset).

electrons present in the relativistic jets. This interaction is expected to produce a progressive enhancement of the X-ray emission in high- z blazars, since the CMB photon density increases as $(1+z)^4$. Using this model, Ighina et al. (2021) found that the space densities of radio-selected (Mao et al. 2017) and X-ray-selected (Ajello et al. 2009) blazars can be nicely reconciled. In this picture, the apparent increase of the space density of X-ray selected blazars at high redshift is only a consequence of the progressive enhancement of their typical X-ray luminosity.

In spite of the similar global behaviour of the two distributions in Fig. 4, we can notice some possible differences. First, the space density peak of the most massive SMBHs hosted by jetted AGNs seems to occur at slightly higher redshift ($z_{\text{peak}} \sim 3$) when compared to that of the entire AGN population ($z_{\text{peak}} \sim 2.2$). In order to better quantify this difference we can fit the jetted AGNs space density (obtained using Eq. 12 with $\Gamma = 10$), as a function of z , with a simple double power law model:

$$n(z) = \frac{2n_0}{\left(\frac{1+z}{1+z_0}\right)^{\gamma_1} + \left(\frac{1+z}{1+z_0}\right)^{\gamma_2}} \quad (14)$$

With γ_1 and γ_2 representing the two slopes, n_0 is a normalization parameter and z_0 represents the break point. The uncertainties are calculated using a Monte Carlo simulation and are given at 68% confidence level. The best fit value of z_0 is 2.98 ± 0.27 . This is not consistent with the total AGN population density peak. This in turn seems to suggest that the comoving space density of the most massive SMBHs hosted by jetted AGNs reach the maximum value about ~ 800 Myr before those hosted by the total AGN population. Another possible difference between the two curves of Fig. 4 is the flatter slope at redshifts below the peak observed in the RL AGNs compared to the total population. This is, however, an uncertain result since we are sampling only a relatively narrow range

of redshifts below $z < 2$. We want to stress here that the evolutionary *shape* of the jetted space density is independent of the choice of the Lorentz bulk factor, which is highly uncertain and can only change the overall normalization of the global evolutionary pattern (unless the average value of Γ changes across the considered range of redshifts).

Finally, we can evaluate the evolution of the fraction of the jetted AGNs hosting the most massive SMBHs with respect to the total population. In Fig. 5 we report the percentage fraction of the jetted AGNs estimated in our work, using three representative values of $\Gamma = [5, 10, 15]$. Clearly, given the uncertainty on the value of Γ , we cannot tightly constrain the absolute value of RL AGNs. However, assuming that the average value of Γ does not change with z , we can establish whether the fraction of jetted AGNs hosting a massive SMBH has changed between $z \sim 1$ up to $z \sim 6$. Fig. 5 seems to suggest a progressive decrease of this fraction by a factor ~ 2 , going from $z \sim 1$ to $z \sim 5$, independently to the assumed average value of Γ . This is in line with what was found by other authors (e.g. Jiang et al. 2007; Kratzer 2014).

In addition, we can compare our result with some independent estimates of the RL fraction published in the literature. In Fig. 5 we report the high-redshift estimates derived by directly counting the known RL AGNs (not necessarily blazars). We consider here only the estimates based on samples with similar optical luminosity limit, namely: $-29 < M_{1450} < -26.8$ (Yang et al. 2016); PS1 $i < 22.6$, at $z \sim 6$ (Bañados et al. 2015); $M_{1450} < -25.5$ (Liu et al. 2021, luminous sample) and with similar *deboosted* radio luminosity limit $f_{1.4\text{GHz}} > 1\text{mJy}$. We want to stress that this method, as mentioned above, could be affected by numerous biases that can be avoided focusing on blazars instead. However, considering all the uncertainties, our results are consistent with the estimates from the literature assuming a Lorentz bulk factor between ≈ 6 and 8 . We can also compare our results with the observed local fraction of RL AGNs. To this end we want to consider an estimate based on a sample with similar properties, since some recent works seem to suggest that the RL fraction may depend on the mass and the luminosity of the SMBH (e.g. Cirasuolo et al. 2003; Jiang et al. 2007; Rafter et al. 2009; Yang et al. 2016). Jiang et al. (2007), in particular, gives an independent estimate of the RL fraction as a function of both luminosity and redshifts. Focusing on $z \sim 1.5$ we find that the *local* RL fraction is estimated to be 10%–20%, consistent with our low-redshift value assuming again a $\Gamma \approx 5$.

6 CONCLUSION

We have assembled a complete and well-defined sample of 380 blazars (FSRQs) with a similar range of optical/radio luminosities ($\lambda L_{1350} \gtrsim 10^{46} \text{ erg s}^{-1}$, $P_{5\text{GHz}} \gtrsim 10^{27} \text{ W Hz}^{-1}$) hosting SMBHs with masses $\gtrsim 10^9 M_\odot$, across a wide redshift interval ($1.5 \leq z \leq 5.5$). We have used this statistically complete sample to infer the evolutionary path of all the jetted AGNs with similar properties, and we have compared the result with the total AGN population, using the most recent QLF available to date (Shen et al. 2020). The findings can be summarized as follow:

- Differently from the overall AGNs population, the jetted AGNs space density shows a peak at a slightly higher redshift ($z \sim 3$ as opposed to $z \sim 2.2$) but not so extreme as the value previously inferred using X-ray selected blazars ($z \sim 4$).
- There is a marginal evidence of a flat density evolution in the jetted AGNs population at $z < 3$ whereas the overall population density strongly decreases.

- The jetted AGNs fraction seems to decrease by a factor of 2 going from $z \sim 1$ to $z \sim 5$.

- Assuming a mean Lorentz bulk factor $\Gamma \approx 5$ the jetted AGNs fraction is overall consistent with the values estimated in the literature in the local Universe (10–20%) and at high redshifts.

The possible differences in the cosmological evolution of SMBHs hosted by jetted and non-jetted AGNs should be investigated more carefully using larger samples of blazars. In particular, in order to establish more accurately the peak position we need to improve the statistics at $z \sim 2$. At the same time, the investigation of any difference in the slope at $z > 2$ between the two populations requires to better sample the very high redshift end of the curve ($z > 5$), where only few blazars have been discovered to date. Sampling this very high- z part of the blazar population is also critical to fully understand the origin of the difference observed between radio and X-ray selected blazars. Indeed, our results seem to rule out the presence of a peak at $z \geq 4$, previously suggested by X-ray selected surveys. As already explained, this discrepancy could be connected to a progressive increase of the X-ray-to-radio luminosity ratio with redshift, possibly caused by the interaction of jet with the photons from the CMB (Ighina et al. 2021). To further test this (and other) hypotheses it is fundamental to significantly increase the statistics at redshift above 5.5 where the effect of CMB is expected to be more and more relevant and where only one blazar has been discovered to date.

Creating sizable samples of blazars at such high redshifts is very challenging given the particular scarcity of these sources. A big leap forward is expected in the next years thanks to the new wide area surveys, covering most of the sky, that will be carried out by the new generation of radio (*Square Kilometre Array*, SKA, and its precursors), X-ray (*extended Röntgen Survey with an Imaging Telescope Array*, eROSITA and Athena) and optical/IR (e.g. the *Vera C. Rubin Observatory* and *Euclid*) telescopes. The joint use of data covering such a large portion of the sky and of the electromagnetic spectrum has been proven to be crucial to efficiently select high- z blazars. In addition, given the extreme faintness of the expected counterparts, a fundamental role will be also played by the incoming large optical/IR telescopes, like *Extremely Large Telescope*, ELT, and *James Webb Space Telescope*, JWST, that will guarantee a reliable spectroscopic follow-up. We are confident that in the near future the same kind of study discussed here will be feasible up to $z \sim 7$ –8 and for less massive objects allowing us to better constrain the global evolution of SMBHs in jetted AGNs and to understand the actual role of the relativistic jets in the global picture.

ACKNOWLEDGEMENTS

The authors would like to thank the referee who provided useful and detailed comments that helped in the manuscript refinement. This work is based on SDSS data. Funding for the Sloan Digital Sky Survey IV has been provided by the Alfred P. Sloan Foundation, the U.S. Department of Energy Office of Science, and the Participating Institutions. SDSS-IV acknowledges support and resources from the Center for High-Performance Computing at the University of Utah. The SDSS web site is www.sdss.org. We acknowledge financial contribution from the agreement ASI-INAF n. I/037/12/0 and n.2017-14-H.0 and from INAF under PRIN SKA/CTA FORECaST.

DATA AVAILABILITY

The data underlying this article are available in the article and in its online supplementary material.

REFERENCES

- Abolfathi B., et al., 2018, *ApJS*, **235**, 42
- Ajello M., et al., 2009, *The Astrophysical Journal*, **699**, 603–625
- Ajello M., et al., 2012, *The Astrophysical Journal*, **751**, 108
- An H., Romani R. W., 2018, *ApJ*, **856**, 105
- An T., et al., 2020, *Nature Communications*, **11**, 143
- Avni Y., Bahcall J. N., 1980, *ApJ*, **235**, 694
- Bañados E., et al., 2015, *The Astrophysical Journal*, **804**, 118
- Belladitta S., et al., 2020, *A&A*, **635**, L7
- Bentz M. C., 2015, AGN Reverberation Mapping ([arXiv:1505.04805](https://arxiv.org/abs/1505.04805))
- Best P. N., Heckman T. M., 2012, *MNRAS*, **421**, 1569
- Best P. N., Kauffmann G., Heckman T. M., Brinchmann J., Charlton S., Ivezic Ž., White S. D. M., 2005, *MNRAS*, **362**, 25
- Blandford R., Meier D., Readhead A., 2019, *ARA&A*, **57**, 467
- Blanton M. R., et al., 2017, *AJ*, **154**, 28
- Browne I. W. A., et al., 2003, *MNRAS*, **341**, 13
- Caccianiga A., et al., 2019, *Monthly Notices of the Royal Astronomical Society*, **484**, 204–217
- Calderone G., Ghisellini G., Colpi M., Dotti M., 2013, *MNRAS*, **431**, 210
- Chambers K. C., et al., 2016, arXiv e-prints, p. [arXiv:1612.05560](https://arxiv.org/abs/1612.05560)
- Cirasuolo M., Magliocchetti M., Celotti A., Danese L., 2003, *MNRAS*, **341**, 993
- Coatman L., Hewett P. C., Banerji M., Richards G. T., Hennawi J. F., Prochaska J. X., 2016, *Monthly Notices of the Royal Astronomical Society*, **465**, 2120–2142
- Condon J. J., Condon M. A., Mitchell K. J., Usher P. D., 1980, *ApJ*, **242**, 486
- Condon J. J., Cotton W. D., Greisen E. W., Yin Q. F., Perley R. A., Taylor G. B., Broderick J. J., 1998, *AJ*, **115**, 1693
- Coppejans R., et al., 2017, *Monthly Notices of the Royal Astronomical Society*, **467**, 2039
- Decarli R., Labita M., Treves A., Falomo R., 2008, *Monthly Notices of the Royal Astronomical Society*, **387**, 1237–1247
- Decarli R., Dotti M., Treves A., 2010, *Monthly Notices of the Royal Astronomical Society*, **413**
- Denney K. D., 2012, *The Astrophysical Journal*, **759**, 44
- Denney K. D., Pogge R. W., Assef R. J., Kochanek C. S., Peterson B. M., Vestergaard M., 2013, *The Astrophysical Journal*, **775**, 60
- Denney K. D., et al., 2016, *The Astrophysical Journal Supplement Series*, **224**, 14
- Evans P. A., et al., 2020, *ApJS*, **247**, 54
- Fanti C., Fanti R., Lari C., Padrielli L., van der Laan H., de Ruiter H., 1977, *A&A*, **61**, 487
- Fine S., Jarvis M. J., Mauch T., 2011, *MNRAS*, **412**, 213
- Fitzpatrick E. L., 1999, *PASP*, **111**, 63
- Ghisellini G., 2015, *Journal of High Energy Astrophysics*, **7**, 163
- Ghisellini G., et al., 2010, *Monthly Notices of the Royal Astronomical Society*, **405**, 387
- Ghisellini G., Celotti A., Tavecchio F., Haardt F., Sbarro T., 2014a, *MNRAS*, **438**, 2694
- Ghisellini G., Sbarro T., Tagliaferri G., Foschini L., Tavecchio F., Ghirlanda G., Braito V., Gehrels N., 2014b, *Monthly Notices of the Royal Astronomical Society: Letters*, **440**, L111
- Gregory P., Scott W., Douglas K., Condon J., 1996, *The Astrophysical Journal Supplement Series*, **103**, 427
- Grier C. J., et al., 2019, *The Astrophysical Journal*, **887**, 38
- Hooper E. J., Impey C. D., Foltz C. B., Hewett P. C., 1995, *ApJ*, **445**, 62
- Hopkins P. F., Richards G. T., Hernquist L., 2007, *ApJ*, **654**, 731
- Ighina L., Caccianiga A., Moretti A., Belladitta S., Della Ceca R., Ballo L., Dallacasa D., 2019, *Monthly Notices of the Royal Astronomical Society*, **489**, 2732–2745
- Ighina L., Caccianiga A., Moretti A., Belladitta S., Della Ceca R., Diana A., 2021, *MNRAS*, **505**, 4120
- Ivezic Ž., et al., 2002, *AJ*, **124**, 2364
- Jiang L., Fan X., Ivezic Ž., Richards G. T., Schneider D. P., Strauss M. A., Kelly B. C., 2007, *The Astrophysical Journal*, **656**, 680
- Kaspi S., Smith P. S., Netzer H., Maoz D., Jannuzi B. T., Giveon U., 2000, *The Astrophysical Journal*, **533**, 631
- Kellermann K. I., Sramek R., Schmidt M., Shaffer D. B., Green R., 1989, *AJ*, **98**, 1195
- Kellermann K. I., Condon J. J., Kimball A. E., Perley R. A., Ivezic Ž., 2016, *ApJ*, **831**, 168
- Kratzer R. M., 2014, PhD thesis, Drexel University
- Leighly K. M., 2004, *The Astrophysical Journal*, **611**, 125–152
- Liu Y., et al., 2021, *ApJ*, **908**, 124
- Ma X., Hopkins P. F., Faucher-Giguère C.-A., Zolman N., Muratov A. L., Kereš D., Quataert E., 2015, *Monthly Notices of the Royal Astronomical Society*, **456**, 2140
- Mao P., Urry C. M., Marchesini E., Landoni M., Massaro F., Ajello M., 2017, *ApJ*, **842**, 87
- Mejía-Restrepo J. E., Trakhtenbrot B., Lira P., Netzer H., Capellupo D. M., 2016, *Monthly Notices of the Royal Astronomical Society*, **460**, 187–211
- Merloni A., 2016, Observing Supermassive Black Holes Across Cosmic Time: From Phenomenology to Physics. Springer International Publishing, Cham, pp 101–143, doi:[10.1007/978-3-319-19416-5_4](https://doi.org/10.1007/978-3-319-19416-5_4), https://doi.org/10.1007/978-3-319-19416-5_4
- Murray N., Chiang J., 1997, *The Astrophysical Journal*, **474**, 91
- Myers S. T., et al., 2003, *MNRAS*, **341**, 1
- Narayan R., McClintock J. E., Tchekhovskoy A., 2014, Energy Extraction from Spinning Black Holes Via Relativistic Jets. Springer International Publishing, Cham, pp 523–535, doi:[10.1007/978-3-319-06349-2_25](https://doi.org/10.1007/978-3-319-06349-2_25), https://doi.org/10.1007/978-3-319-06349-2_25
- O’Dea C. P., 1998, *PASP*, **110**, 493
- Padovani P., 2017, *Nature Astronomy*, **1**, 0194
- Rafter S. E., Crenshaw D. M., Wiita P. J., 2009, *AJ*, **137**, 42
- Richards G. T., et al., 2011, *Astronomical Journal*, **141**, 1
- Romani R. W., 2006, *AJ*, **132**, 1959
- Romani R. W., Sowards-Emmerd D., Greenhill L., Michelson P., 2004, *ApJ*, **610**, L9
- Runnoe J. C., Brotherton M. S., DiPompeo M. A., Shang Z., 2014, *Monthly Notices of the Royal Astronomical Society*, **438**, 3263
- Savolainen T., Homan D. C., Hovatta T., Kadler M., Kovalev Y. Y., Lister M. L., Ros E., Zensus J. A., 2010, *A&A*, **512**, A24
- Sbarro T., Ghisellini G., Tagliaferri G., Foschini L., Nardini M., Tavecchio F., Gehrels N., 2015, *MNRAS*, **446**, 2483
- Shen Y., Liu X., 2012, *The Astrophysical Journal*, **753**, 125
- Shen Y., et al., 2011, *The Astrophysical Journal Supplement Series*, **194**, 45
- Shen X., Hopkins P. F., Faucher-Giguère C.-A., Alexander D. M., Richards G. T., Ross N. P., Hickox R. C., 2020, *Monthly Notices of the Royal Astronomical Society*, **495**, 3252–3275
- Singal A. K., 2016, *ApJ*, **827**, 66
- Smith M. G., Wright A. E., 1980, *MNRAS*, **191**, 871
- Sramek R. A., Weedman D. W., 1980, *ApJ*, **238**, 435
- Stern D., Djorgovski S. G., Perley R. A., de Carvalho R. R., Wall J. V., 2000, *AJ*, **119**, 1526
- Sun M., Xue Y., Richards G. T., Trump J. R., Shen Y., Brandt W. N., Schneider D. P., 2018, *The Astrophysical Journal*, **854**, 128
- Tchekhovskoy A., Narayan R., McKinney J. C., 2011, *MNRAS*, **418**, L79
- Thorne K. S., 1974, *ApJ*, **191**, 507
- Ueda Y., Akiyama M., Hasinger G., Miyaji T., Watson M. G., 2014, *The Astrophysical Journal*, **786**, 104
- Urry C. M., Padovani P., 1995, *Publications of the Astronomical Society of the Pacific*, **107**, 803
- Valiante R., Agarwal B., Habouzit M., Pezzulli E., 2017, *Publ. Astron. Soc. Australia*, **34**, e031
- Vanden Berk D. E., et al., 2001, *AJ*, **122**, 549
- Vestergaard M., Peterson B. M., 2006, *The Astrophysical Journal*, **641**, 689–709

- Vito F., et al., 2018, [MNRAS, 473, 2378](#)
Volonteri M., 2010, [A&ARv, 18, 279](#)
Volonteri M., Haardt F., Ghisellini G., Ceca R. D., 2011, [Monthly Notices of the Royal Astronomical Society](#), 416, 216
Wright E. L., et al., 2010, [AJ, 140, 1868](#)
Yang J., et al., 2016, [The Astrophysical Journal](#), 829, 33
Zhu B.-T., Zhang L., Fang J., 2019, [ApJ, 873, 120](#)
della Ceca R., Lamorani G., Maccacaro T., Wolter A., Griffiths R., Stocke J. T., Setti G., 1994, [ApJ, 430, 533](#)

Table A1: Properties of the FSRQs in our sample. **column 1:** source name; **column 2:** redshift; **column 3:** total extinction in the V-band; **column 4:** magnitude in the *r*-filter ; **column 5:** radio flux density measured at 5GHz; **columns 6 and 7:** CIV line dispersion and FWHM; **column 8:** continuum luminosity at 1350Å **column 9:** CIV λ 1549 line luminosity; **column 10:** bolometric luminosity, calculated assuming a bolometric correction $K_{bol}(1350\text{\AA}) = 4.5$; **columns 11 and 12:** SMBH mass, estimated using the VP06 relations (see text); **columns 13 and 14:** Eddington ratios calculated using the masses derived from the line dispersion and the FWHM, respectively.

name	z	A_V	<i>r</i> -mag	$S_{5\text{GHz}}$ (mJy)	σ_l (km s $^{-1}$)	FWHM (km s $^{-1}$)	LogL ₁₃₅₀ (erg s $^{-1}$)	LogL _{CIV} (erg s $^{-1}$)	LogL _{bol} (erg s $^{-1}$)	LogM $_\sigma$ (M_\odot)	LogM _{FWHM} (M_\odot)	Log λ_{Edd} [σ_l]	Log λ_{Edd} [FWHM]
GB6J000026+030706	2.35	0.148	18.74	91	3091 ± 161	5613 ± 373	46.515 ± 0.005	44.487 ± 0.011	47.168 ± 0.005	9.04 ± 0.04	9.49 ± 0.06	0.02 ± 0.04	-0.42 ± 0.06
GB6J000345+160536	2.31	0.198	19.49	109	4802 ± 539	4838 ± 291	46.383 ± 0.006	44.481 ± 0.012	47.036 ± 0.006	9.36 ± 0.09	9.29 ± 0.05	-0.42 ± 0.09	-0.36 ± 0.05
GB6J000519+052349	1.90	0.212	16.23	303	-	-	-	-	-	-	-	-	-
GB6J000649+242232	1.68	0.276	18.79	189	4390 ± 1472	4064 ± 465	46.260 ± 0.005	44.885 ± 0.667	46.913 ± 0.005	9.21 ± 0.23	9.08 ± 0.11	-0.40 ± 0.23	-0.26 ± 0.12
GB6J000917+062549	2.69	0.292	19.42	156	3064 ± 95	4451 ± 261	46.323 ± 0.005	44.104 ± 0.014	46.977 ± 0.005	8.93 ± 0.03	9.19 ± 0.05	-0.06 ± 0.03	-0.31 ± 0.05
GB6J000942+151357	2.24	0.252	19.74	121	3415 ± 508	3484 ± 389	45.746 ± 0.017	44.315 ± 0.014	46.399 ± 0.017	8.72 ± 0.09	8.67 ± 0.10	-0.42 ± 0.09	-0.37 ± 0.10
GB6J001033+172437	1.60	0.196	16.70	989	-	-	-	-	-	-	-	-	-
GB6J001115+144608	4.96	0.242	19.62	31	3310 ± 138	7548 ± 322	47.326 ± 0.004	45.240 ± 0.012	47.979 ± 0.004	9.53 ± 0.04	10.18 ± 0.04	0.35 ± 0.04	-0.30 ± 0.04
GB6J001144+292820	2.63	0.225	19.24	107	2308 ± 113	3097 ± 358	46.450 ± 0.008	44.554 ± 0.012	47.103 ± 0.008	8.76 ± 0.04	8.94 ± 0.10	0.25 ± 0.04	0.06 ± 0.10
GB6J001154+083359	2.20	0.474	19.84	87	3975 ± 119	4258 ± 405	45.819 ± 0.010	44.195 ± 0.013	46.472 ± 0.010	8.89 ± 0.03	8.88 ± 0.08	-0.52 ± 0.03	-0.51 ± 0.09
GB6J001307+205335	3.53	0.199	17.80	41	-	-	-	-	-	-	-	-	-
GB6J001837+041532	2.70	0.137	19.78	142	4693 ± 1118	3290 ± 431	45.911 ± 0.018	44.715 ± 0.025	46.564 ± 0.018	9.09 ± 0.17	8.71 ± 0.12	-0.62 ± 0.17	-0.24 ± 0.12
GB6J002121+155127	3.70	0.209	19.64	35	4796 ± 210	3677 ± 206	46.440 ± 0.011	44.945 ± 0.012	47.093 ± 0.011	9.38 ± 0.04	9.08 ± 0.05	-0.39 ± 0.04	-0.09 ± 0.05
GB6J002903+050931	1.63	0.128	18.53	377	4952 ± 398	5032 ± 301	45.958 ± 0.013	44.484 ± 0.012	46.611 ± 0.013	9.16 ± 0.07	9.10 ± 0.05	-0.65 ± 0.07	-0.59 ± 0.05
GB6J003443+275423	2.96	0.256	18.39	587	2907 ± 88	2903 ± 369	46.877 ± 0.004	45.214 ± 0.009	47.530 ± 0.004	9.18 ± 0.03	9.11 ± 0.12	0.25 ± 0.03	0.32 ± 0.12
GB6J003544+143803	2.45	0.248	19.37	328	7775 ± 682	3871 ± 301	46.273 ± 0.008	44.758 ± 0.014	46.926 ± 0.008	9.72 ± 0.08	9.04 ± 0.07	-0.89 ± 0.08	-0.21 ± 0.07
GB6J003759+160629	3.34	0.203	20.60	77	3789 ± 742	3677 ± 590	45.711 ± 0.036	44.474 ± 0.015	46.364 ± 0.036	8.79 ± 0.10	8.70 ± 0.14	-0.53 ± 0.10	-0.43 ± 0.15
GB6J010037+334513	2.14	0.278	19.68	119	3748 ± 68	6774 ± 360	45.865 ± 0.013	44.766 ± 0.006	46.518 ± 0.013	8.87 ± 0.02	9.31 ± 0.05	-0.45 ± 0.02	-0.89 ± 0.04
GB6J010838+013516	2.10	0.126	18.09	4180	4421 ± 544	3290 ± 539	46.772 ± 0.004	44.973 ± 0.015	47.426 ± 0.004	9.49 ± 0.08	9.16 ± 0.14	-0.17 ± 0.08	0.16 ± 0.14
GB6J010838+140428	1.70	0.193	19.01	132	3224 ± 81	2322 ± 227	46.287 ± 0.007	44.509 ± 0.009	46.941 ± 0.007	8.96 ± 0.02	8.60 ± 0.08	-0.12 ± 0.02	0.24 ± 0.09
GB6J011114+171320	2.20	0.260	19.51	99	5512 ± 863	3871 ± 372	46.216 ± 0.007	44.708 ± 0.015	46.869 ± 0.007	9.39 ± 0.12	9.01 ± 0.09	-0.62 ± 0.12	-0.24 ± 0.09
GB6J011163+290406	3.28	0.302	18.69	68	4129 ± 243	2710 ± 335	46.561 ± 0.009	45.097 ± 0.010	47.215 ± 0.009	9.32 ± 0.06	8.88 ± 0.11	-0.20 ± 0.05	0.23 ± 0.11
GB6J012129+112702	2.49	0.206	17.23	194	3201 ± 76	3290 ± 483	46.987 ± 0.004	44.767 ± 0.014	47.640 ± 0.004	9.32 ± 0.02	9.28 ± 0.14	0.22 ± 0.02	0.26 ± 0.14
GB6J012202+030951	4.00	0.161	20.86	96	-	5800 ± 2000	46.450 ± 0.070	-	47.103 ± 0.070	-	9.52 ± 0.39	-	-0.51 ± 0.39
GB6J012238+250238	2.02	0.408	19.07	764	3932 ± 460	5032 ± 485	46.028 ± 0.012	44.981 ± 0.012	46.681 ± 0.012	8.99 ± 0.09	9.14 ± 0.08	-0.41 ± 0.09	-0.56 ± 0.09
GB6J012642+255902	2.36	0.458	18.13	1303	3628 ± 48	3871 ± 560	46.839 ± 0.003	45.179 ± 0.012	47.492 ± 0.003	9.35 ± 0.01	9.34 ± 0.17	0.04 ± 0.01	0.05 ± 0.17
GB6J012921+310303	3.56	0.265	19.48	74	8055 ± 584	4838 ± 439	46.583 ± 0.009	44.853 ± 0.013	47.236 ± 0.009	9.91 ± 0.06	9.40 ± 0.08	-0.78 ± 0.06	-0.26 ± 0.08
GB6J013942+175253	2.72	0.296	18.71	301	4089 ± 258	3097 ± 263	46.574 ± 0.005	45.037 ± 0.009	47.227 ± 0.005	9.32 ± 0.05	9.01 ± 0.08	-0.19 ± 0.05	0.12 ± 0.08
GB6J015235+335037	2.41	0.261	18.23	611	3442 ± 47	6193 ± 183	46.733 ± 0.005	44.819 ± 0.008	47.386 ± 0.005	9.25 ± 0.01	9.69 ± 0.03	0.03 ± 0.01	-0.41 ± 0.03
GB6J015855+130705	1.89	0.324	18.91	272	3688 ± 246	4451 ± 300	46.358 ± 0.022	44.748 ± 0.011	47.011 ± 0.022	9.11 ± 0.06	9.21 ± 0.06	-0.20 ± 0.06	-0.30 ± 0.06
GB6J015923+310648	2.25	0.263	18.35	190	6628 ± 1129	3097 ± 1207	46.572 ± 0.005	45.030 ± 0.176	47.225 ± 0.005	9.74 ± 0.13	9.00 ± 0.21	-0.61 ± 0.13	0.12 ± 0.21
GB6J020310+263246	3.35	0.387	19.58	77	3819 ± 138	3097 ± 230	46.498 ± 0.008	45.127 ± 0.008	47.151 ± 0.008	9.22 ± 0.03	8.97 ± 0.06	-0.17 ± 0.03	0.09 ± 0.06
GB6J020521+241624	2.45	0.424	19.28	243	4293 ± 441	2516 ± 280	46.319 ± 0.005	44.847 ± 0.016	46.972 ± 0.005	9.22 ± 0.09	8.69 ± 0.10	-0.35 ± 0.09	0.18 ± 0.10

Continued on next page

	name	z	A_V	r-mag	$S_{5\text{GHz}}$ (mJy)	σ_l (km s $^{-1}$)	FWHM (km s $^{-1}$)	$\log \lambda L_{1350}$ (erg s $^{-1}$)	$\log L_{CIV}$ (erg s $^{-1}$)	$\log L_{\text{bol}}$ (erg s $^{-1}$)	$\log M_\sigma$ (M_\odot)	$\log M_{\text{FWHM}}$ (M_\odot)	$\log \lambda_{\text{Edd}}$ [σ_l]	$\log \lambda_{\text{Edd}}$ [FWHM]
GB6J021436+015702	3.28	0.170	19.48	103	2762 ± 80	6387 ± 206	46.272 ± 0.016	44.407 ± 0.009	46.926 ± 0.016	8.82 ± 0.03	9.47 ± 0.03	0.01 ± 0.03	-0.65 ± 0.03	
GB6J021748+014451	1.72	0.173	16.18	1419	-	-	-	-	-	-	-	-	-	
GB6J024917+061957	1.88	0.590	17.97	620	-	-	-	-	-	-	-	-	-	
GB6J034423+155934	2.28	1.334	19.94	313	-	-	-	-	-	-	-	-	-	
GB6J040738+001713	3.70	0.989	19.66	40	-	-	-	-	-	-	-	-	-	
GB6J042457+080533	3.08	0.888	19.87	163	-	-	-	-	-	-	-	-	-	
GB6J042834+173228	3.32	1.310	18.23	175	-	-	-	-	-	-	-	-	-	
GB6J044907+112125	2.15	1.190	19.95	794	-	-	-	-	-	-	-	-	-	
GB6J051340+010028	2.68	0.566	19.34	368	-	-	-	-	-	-	-	-	-	
GB6J072201+372235	1.63	0.345	17.81	302	-	-	-	-	-	-	-	-	-	
GB6J072622+412438	1.80	0.447	19.15	120	2474 ± 90	5613 ± 241	46.145 ± 0.013	44.308 ± 0.009	46.798 ± 0.013	8.65 ± 0.03	9.30 ± 0.04	0.04 ± 0.03	-0.60 ± 0.04	
GB6J073051+404954	2.50	0.361	18.97	473	6626 ± 373	4451 ± 363	46.318 ± 0.007	45.048 ± 0.009	46.971 ± 0.007	9.60 ± 0.05	9.19 ± 0.07	-0.73 ± 0.05	-0.31 ± 0.07	
GB6J073631+284032	3.63	0.268	20.08	82	2134 ± 78	5419 ± 470	45.715 ± 0.041	43.774 ± 0.016	46.368 ± 0.041	8.30 ± 0.04	9.04 ± 0.09	-0.03 ± 0.04	-0.77 ± 0.08	
GB6J074308+394108	1.70	0.317	18.47	416	2841 ± 174	3677 ± 278	46.273 ± 0.008	44.751 ± 0.010	46.927 ± 0.008	8.84 ± 0.05	9.00 ± 0.06	-0.02 ± 0.05	-0.17 ± 0.06	
GB6J074625+254906	2.98	0.246	19.50	476	4426 ± 2610	5419 ± 796	46.436 ± 0.008	44.743 ± 0.616	47.089 ± 0.008	9.31 ± 0.31	9.42 ± 0.21	-0.32 ± 0.31	-0.43 ± 0.21	
GB6J075009+501505	2.10	0.317	19.40	229	4473 ± 183	2322 ± 228	46.013 ± 0.015	44.550 ± 0.009	46.667 ± 0.015	9.10 ± 0.04	8.46 ± 0.09	-0.53 ± 0.04	0.11 ± 0.08	
GB6J075020+481458	1.96	0.298	18.41	902	4490 ± 665	4451 ± 402	46.505 ± 0.014	44.837 ± 0.014	47.158 ± 0.014	9.36 ± 0.12	9.28 ± 0.09	-0.30 ± 0.12	-0.23 ± 0.09	
GB6J075039+192003	1.92	0.215	18.32	124	4312 ± 357	10064 ± 1103	46.440 ± 0.011	44.551 ± 0.016	47.093 ± 0.011	9.29 ± 0.07	9.96 ± 0.11	-0.30 ± 0.07	-0.97 ± 0.11	
GB6J075303+423131	3.59	0.244	17.63	450	4643 ± 868	2710 ± 306	47.241 ± 0.002	45.502 ± 0.017	47.894 ± 0.002	9.78 ± 0.14	9.24 ± 0.10	0.01 ± 0.14	0.55 ± 0.10	
GB6J075529+232919	3.69	0.327	20.58	81	3703 ± 105	3484 ± 266	46.019 ± 0.026	44.524 ± 0.011	46.672 ± 0.026	8.94 ± 0.03	8.81 ± 0.07	-0.37 ± 0.03	-0.24 ± 0.07	
GB6J075837+135756	2.20	0.171	17.80	88	4393 ± 279	3871 ± 289	46.690 ± 0.005	45.258 ± 0.009	47.343 ± 0.005	9.44 ± 0.05	9.26 ± 0.07	-0.20 ± 0.05	-0.02 ± 0.07	
GB6J080244+525546	2.01	0.204	19.52	120	4610 ± 1064	2710 ± 844	46.100 ± 0.022	44.862 ± 0.030	46.753 ± 0.022	9.17 ± 0.14	8.64 ± 0.32	-0.52 ± 0.14	0.01 ± 0.34	
GB6J080306+203816	2.67	0.195	19.96	75	4215 ± 233	5613 ± 390	46.095 ± 0.011	44.488 ± 0.010	46.748 ± 0.011	9.09 ± 0.05	9.27 ± 0.06	-0.44 ± 0.05	-0.62 ± 0.06	
GB6J080634+450439	2.10	0.228	19.62	424	3715 ± 132	5419 ± 357	46.251 ± 0.006	44.580 ± 0.007	46.904 ± 0.006	9.06 ± 0.03	9.32 ± 0.06	-0.26 ± 0.03	-0.52 ± 0.06	
GB6J080711+131741	3.72	0.142	20.14	36	5157 ± 248	4838 ± 272	46.267 ± 0.014	44.659 ± 0.014	46.920 ± 0.014	9.36 ± 0.04	9.23 ± 0.05	-0.54 ± 0.04	-0.41 ± 0.05	
GB6J081025+101050	2.50	0.136	17.54	141	3319 ± 67	5806 ± 381	46.824 ± 0.004	44.783 ± 0.008	47.477 ± 0.004	9.27 ± 0.02	9.68 ± 0.06	0.11 ± 0.02	-0.31 ± 0.06	
GB6J081303+254215	2.02	0.208	18.80	393	2514 ± 68	4258 ± 252	46.392 ± 0.015	44.599 ± 0.011	47.046 ± 0.015	8.80 ± 0.02	9.19 ± 0.05	0.15 ± 0.03	-0.24 ± 0.05	
GB6J081710+235225	1.73	0.256	18.96	147	1043 ± 38	2322 ± 109	46.242 ± 0.010	43.960 ± 0.016	46.896 ± 0.010	7.96 ± 0.03	8.58 ± 0.04	0.84 ± 0.03	0.21 ± 0.04	
GB6J082106+310756	2.61	0.181	17.06	161	3575 ± 66	4838 ± 450	47.242 ± 0.002	45.287 ± 0.007	47.895 ± 0.002	9.55 ± 0.02	9.75 ± 0.08	0.24 ± 0.02	0.05 ± 0.08	
GB6J082154+285746	2.80	0.147	19.98	209	4408 ± 297	3677 ± 966	45.989 ± 0.013	44.586 ± 0.016	46.643 ± 0.013	9.07 ± 0.06	8.85 ± 0.26	-0.53 ± 0.06	-0.30 ± 0.27	
GB6J082329+061148	2.80	0.119	17.85	70	4098 ± 78	5419 ± 277	46.995 ± 0.004	45.133 ± 0.006	47.648 ± 0.004	9.54 ± 0.02	9.72 ± 0.04	0.01 ± 0.02	-0.17 ± 0.04	
GB6J082341+292842	2.37	0.168	18.82	480	2583 ± 142	2322 ± 339	46.234 ± 0.009	44.855 ± 0.014	46.887 ± 0.009	8.74 ± 0.05	8.58 ± 0.12	0.05 ± 0.05	0.21 ± 0.14	
GB6J082427+234112	2.61	0.192	18.76	87	3623 ± 248	5806 ± 358	46.452 ± 0.007	44.689 ± 0.010	47.105 ± 0.007	9.15 ± 0.06	9.49 ± 0.06	-0.14 ± 0.06	-0.48 ± 0.06	
GB6J082706+105220	2.28	0.191	18.95	167	3494 ± 123	4838 ± 551	46.330 ± 0.008	44.970 ± 0.008	46.984 ± 0.008	9.05 ± 0.03	9.26 ± 0.10	-0.17 ± 0.03	-0.38 ± 0.16	
GB6J083031+052002	2.22	0.138	18.37	127	3185 ± 67	2322 ± 230	46.649 ± 0.005	45.186 ± 0.011	47.303 ± 0.005	9.14 ± 0.02	8.80 ± 0.09	0.06 ± 0.02	0.41 ± 0.05	
GB6J083249+155413	2.42	0.190	18.36	274	4096 ± 239	5806 ± 210	46.623 ± 0.004	44.897 ± 0.010	47.276 ± 0.004	9.34 ± 0.05	9.58 ± 0.03	-0.17 ± 0.05	-0.40 ± 0.05	
GB6J083313+112400	2.98	0.154	18.32	294	5935 ± 751	3871 ± 336	46.709 ± 0.006	45.373 ± 0.014	47.363 ± 0.006	9.71 ± 0.10	9.27 ± 0.08	-0.45 ± 0.10	-0.01 ± 0.08	
GB6J083322+095956	3.71	0.242	18.82	93	2551 ± 81	4645 ± 480	46.652 ± 0.008	44.689 ± 0.011	47.305 ± 0.008	8.95 ± 0.03	9.40 ± 0.10	0.26 ± 0.03	-0.19 ± 0.10	
GB6J083548+182519	4.41	0.141	21.18	40	2191 ± 89	5032 ± 211	46.104 ± 0.029	44.497 ± 0.016	46.757 ± 0.029	8.53 ± 0.04	9.18 ± 0.04	0.13 ± 0.04	-0.52 ± 0.04	
GB6J083720+582514	2.10	0.266	17.86	717	3482 ± 57	6774 ± 250	46.817 ± 0.006	44.854 ± 0.008	47.470 ± 0.006	9.31 ± 0.01	9.81 ± 0.03	0.06 ± 0.01	-0.44 ± 0.03	
GB6J083852+115119	2.30	0.207	19.41	82	3223 ± 165	4451 ± 404	46.177 ± 0.012	44.671 ± 0.012	46.830 ± 0.012	8.90 ± 0.05	9.11 ± 0.08	-0.17 ± 0.05	-0.38 ± 0.08	

Continued on next page

The evolution of the heaviest SMBHs in jetted AGNs

name	z	A_V	r-mag	$S_{5\text{GHz}}$ (mJy)	σ_l (km s $^{-1}$)	FWHM (km s $^{-1}$)	Log λL_{1350} (erg s $^{-1}$)	Log L_{CIV} (erg s $^{-1}$)	Log L_{bol} (erg s $^{-1}$)	Log M_σ (M $_\odot$)	Log M_{FWHM} (M $_\odot$)	Log λ_{Edd} [σ_l]	Log λ_{Edd} [FWHM]
GB6J111231+313547	2.44	0.083	19.34	108	5955 ± 336	5419 ± 529	46.041 ± 0.012	44.574 ± 0.011	46.694 ± 0.012	9.36 ± 0.05	9.21 ± 0.09	-0.77 ± 0.05	-0.62 ± 0.09
GB6J111239+344642	1.96	0.090	19.30	216	5784 ± 946	3290 ± 375	46.159 ± 0.014	44.542 ± 0.018	46.812 ± 0.014	9.40 ± 0.16	8.84 ± 0.10	-0.69 ± 0.16	-0.13 ± 0.16
GB6J111701+131118	3.63	0.096	18.36	45	6054 ± 462	3097 ± 462	46.815 ± 0.007	45.077 ± 0.010	47.468 ± 0.007	9.79 ± 0.07	9.13 ± 0.13	-0.42 ± 0.07	0.23 ± 0.13
GB6J111753+412014	2.22	0.080	19.47	237	2833 ± 75	3484 ± 491	46.132 ± 0.011	44.950 ± 0.013	46.785 ± 0.011	8.76 ± 0.02	8.87 ± 0.13	-0.08 ± 0.02	-0.19 ± 0.13
GB6J111857+123442	2.13	0.099	18.48	1820	4108 ± 794	2516 ± 456	46.439 ± 0.011	45.039 ± 0.649	47.092 ± 0.011	9.25 ± 0.10	8.75 ± 0.19	-0.26 ± 0.10	0.24 ± 0.19
GB6J111914+600459	2.65	0.030	17.14	170	4696 ± 101	5419 ± 611	47.177 ± 0.003	45.457 ± 0.007	47.830 ± 0.003	9.76 ± 0.02	9.81 ± 0.10	-0.03 ± 0.02	-0.08 ± 0.10
GB6J112338+052053	2.18	0.204	19.10	85	3932 ± 340	4838 ± 366	46.189 ± 0.011	44.846 ± 0.010	46.842 ± 0.011	9.08 ± 0.08	9.19 ± 0.07	-0.34 ± 0.08	-0.45 ± 0.07
GB6J112340+155358	3.39	0.109	20.38	62	3729 ± 774	3677 ± 1137	45.917 ± 0.029	44.713 ± 0.020	46.571 ± 0.029	8.89 ± 0.11	8.81 ± 0.28	-0.42 ± 0.11	-0.34 ± 0.28
GB6J112542+000111	1.70	0.157	17.56	131	4184 ± 769	1935 ± 213	46.535 ± 0.006	45.269 ± 0.018	47.188 ± 0.006	9.32 ± 0.12	8.58 ± 0.10	-0.23 ± 0.12	0.51 ± 0.10
GB6J112554+261017	2.34	0.062	18.22	1176	3489 ± 142	3677 ± 415	46.445 ± 0.007	44.893 ± 0.010	47.098 ± 0.007	9.11 ± 0.04	9.09 ± 0.10	-0.11 ± 0.03	-0.09 ± 0.10
GB6J112651+062605	2.74	0.240	19.23	427	7482 ± 483	6000 ± 301	46.365 ± 0.008	44.663 ± 0.010	47.018 ± 0.008	9.73 ± 0.05	9.47 ± 0.04	-0.81 ± 0.05	-0.55 ± 0.04
GB6J112657+451557	1.81	0.094	17.19	360	3227 ± 106	6000 ± 338	46.875 ± 0.007	45.009 ± 0.007	47.529 ± 0.007	9.27 ± 0.03	9.74 ± 0.05	0.16 ± 0.03	-0.31 ± 0.05
GB6J112739+565013	2.89	0.046	19.59	448	5293 ± 508	2516 ± 305	46.292 ± 0.009	44.859 ± 0.012	46.945 ± 0.009	9.39 ± 0.09	8.68 ± 0.11	-0.55 ± 0.08	0.17 ± 0.11
GB6J112850+232603	3.04	0.066	18.33	109	4318 ± 148	3097 ± 390	46.576 ± 0.005	45.134 ± 0.008	47.229 ± 0.005	9.37 ± 0.03	9.01 ± 0.11	-0.24 ± 0.03	0.12 ± 0.11
GB6J112907+164327	2.00	0.115	17.84	171	4336 ± 253	5032 ± 415	46.543 ± 0.007	44.810 ± 0.009	47.197 ± 0.007	9.35 ± 0.04	9.41 ± 0.08	-0.26 ± 0.04	-0.32 ± 0.08
GB6J112913+095157	1.52	0.168	17.32	367	3831 ± 603	3871 ± 401	46.811 ± 0.003	45.057 ± 0.014	47.464 ± 0.003	9.39 ± 0.10	9.33 ± 0.09	-0.02 ± 0.10	0.04 ± 0.09
GB6J113054+381510	1.73	0.098	18.75	769	3073 ± 104	4258 ± 334	46.262 ± 0.010	44.457 ± 0.009	46.915 ± 0.010	8.90 ± 0.03	9.12 ± 0.07	-0.09 ± 0.03	-0.30 ± 0.07
GB6J113223+445514	2.46	0.110	19.74	176	3689 ± 86	4451 ± 561	45.952 ± 0.014	44.659 ± 0.010	46.606 ± 0.014	8.90 ± 0.02	8.99 ± 0.11	-0.39 ± 0.02	-0.49 ± 0.11
GB6J113720+293537	2.65	0.101	19.56	87	3795 ± 195	1742 ± 174	46.185 ± 0.012	44.479 ± 0.016	46.838 ± 0.012	9.05 ± 0.04	8.30 ± 0.10	-0.31 ± 0.05	0.44 ± 0.10
GB6J114156+494506	2.81	0.078	19.90	113	3549 ± 179	2129 ± 297	46.107 ± 0.012	44.784 ± 0.010	46.760 ± 0.012	8.95 ± 0.04	8.43 ± 0.12	-0.29 ± 0.05	0.23 ± 0.12
GB6J114340+661944	2.58	0.047	19.82	115	4347 ± 88	11032 ± 301	45.987 ± 0.020	44.554 ± 0.008	46.640 ± 0.020	9.06 ± 0.02	9.80 ± 0.03	-0.52 ± 0.02	-1.26 ± 0.03
GB6J114342+663329	2.33	0.047	19.16	245	4637 ± 222	3097 ± 705	45.917 ± 0.017	44.712 ± 0.042	46.571 ± 0.017	9.08 ± 0.04	8.66 ± 0.21	-0.61 ± 0.04	-0.19 ± 0.21
GB6J114814+525854	3.17	0.077	20.07	65	5549 ± 768	2516 ± 407	46.100 ± 0.018	44.690 ± 0.015	46.753 ± 0.018	9.33 ± 0.12	8.57 ± 0.16	-0.68 ± 0.12	0.08 ± 0.16
GB6J114856+525432	1.63	0.080	16.55	288	4355 ± 98	4838 ± 205	46.799 ± 0.005	45.110 ± 0.009	47.452 ± 0.005	9.49 ± 0.02	9.51 ± 0.04	-0.14 ± 0.02	-0.16 ± 0.04
GB6J120140+111453	2.30	0.093	19.64	160	6167 ± 729	2516 ± 936	45.945 ± 0.013	44.383 ± 0.121	46.598 ± 0.013	9.34 ± 0.13	8.49 ± 0.42	-0.84 ± 0.13	0.01 ± 0.42
GB6J120436+522844	2.73	0.086	18.29	213	5912 ± 425	1935 ± 259	46.341 ± 0.008	44.985 ± 0.011	46.994 ± 0.008	9.51 ± 0.06	8.47 ± 0.12	-0.62 ± 0.06	0.42 ± 0.12
GB6J120501+430024	2.96	0.056	18.91	64	5046 ± 512	5032 ± 341	46.658 ± 0.006	45.056 ± 0.012	47.311 ± 0.006	9.54 ± 0.08	9.47 ± 0.06	-0.33 ± 0.08	-0.26 ± 0.06
GB6J120636+394051	1.52	0.144	18.65	190	2297 ± 75	4451 ± 235	46.205 ± 0.009	44.509 ± 0.011	46.858 ± 0.009	8.62 ± 0.03	9.13 ± 0.05	0.14 ± 0.03	-0.37 ± 0.05
GB6J120726+275502	2.18	0.088	18.77	457	3971 ± 295	4645 ± 378	46.470 ± 0.007	44.819 ± 0.013	47.123 ± 0.007	9.24 ± 0.07	9.30 ± 0.08	-0.21 ± 0.07	-0.28 ± 0.08
GB6J121107+182033	1.50	0.138	18.71	381	3712 ± 228	6193 ± 518	45.916 ± 0.020	44.352 ± 0.014	46.569 ± 0.020	8.88 ± 0.05	9.26 ± 0.08	-0.42 ± 0.05	-0.79 ± 0.08
GB6J121254+245337	2.39	0.104	19.03	91	2149 ± 79	4258 ± 316	46.422 ± 0.008	44.233 ± 0.011	47.075 ± 0.008	8.68 ± 0.03	9.20 ± 0.07	0.30 ± 0.03	-0.23 ± 0.07
GB6J121422+513350	3.29	0.100	18.94	41	4204 ± 141	2903 ± 426	46.365 ± 0.011	44.952 ± 0.008	47.019 ± 0.011	9.23 ± 0.03	8.84 ± 0.13	-0.31 ± 0.03	0.08 ± 0.13
GB6J121547+642225	3.23	0.116	18.59	79	3298 ± 154	4258 ± 335	46.835 ± 0.004	45.040 ± 0.010	47.488 ± 0.004	9.27 ± 0.04	9.42 ± 0.07	0.12 ± 0.04	-0.03 ± 0.07
GB6J121710+583523	2.55	0.072	19.06	306	4324 ± 814	2322 ± 229	46.394 ± 0.008	45.087 ± 0.017	47.047 ± 0.008	9.27 ± 0.14	8.66 ± 0.09	-0.32 ± 0.14	0.29 ± 0.09
GB6J121732+330536	2.61	0.058	18.35	117	5814 ± 404	1742 ± 258	46.780 ± 0.005	45.086 ± 0.016	47.433 ± 0.005	9.73 ± 0.06	8.62 ± 0.14	-0.40 ± 0.06	0.72 ± 0.14
GB6J122657+434101	2.01	0.090	19.23	154	3794 ± 135	4064 ± 349	46.241 ± 0.018	44.416 ± 0.009	46.894 ± 0.018	9.08 ± 0.03	9.07 ± 0.07	-0.28 ± 0.03	-0.27 ± 0.07
GB6J122729+135627	3.35	0.153	20.09	89	1798 ± 43	2129 ± 238	46.189 ± 0.016	44.720 ± 0.017	46.842 ± 0.016	8.40 ± 0.02	8.48 ± 0.11	0.34 ± 0.02	0.27 ± 0.10
GB6J122825+312841	2.19	0.078	15.84	345	4192 ± 45	10258 ± 490	47.527 ± 0.003	45.156 ± 0.007	48.180 ± 0.003	9.84 ± 0.01	10.55 ± 0.04	0.24 ± 0.01	-0.47 ± 0.04
GB6J122847+370610	1.52	0.063	18.17	856	2274 ± 55	2129 ± 238	46.244 ± 0.010	44.846 ± 0.012	46.897 ± 0.010	8.63 ± 0.02	8.51 ± 0.10	0.16 ± 0.02	0.29 ± 0.11
GB6J122851+485813	1.72	0.064	18.62	350	3159 ± 107	2710 ± 246	45.289 ± 0.059	43.990 ± 0.013	45.942 ± 0.059	8.41 ± 0.04	8.21 ± 0.09	-0.57 ± 0.04	-0.37 ± 0.09
GB6J123223+195928	2.61	0.143	20.01	74	2723 ± 119	2129 ± 274	46.179 ± 0.010	44.552 ± 0.015	46.832 ± 0.010	8.75 ± 0.04	8.47 ± 0.13	-0.02 ± 0.04	0.26 ± 0.13

Continued on next page

	name	z	A_V	r-mag	$S_{5\text{GHz}}$ (mJy)	σ_l (km s $^{-1}$)	FWHM (km s $^{-1}$)	$\log \lambda L_{1350}$ (erg s $^{-1}$)	$\log L_{CIV}$ (erg s $^{-1}$)	$\log L_{\text{bol}}$ (erg s $^{-1}$)	$\log M_\sigma$ (M_\odot)	$\log M_{\text{FWHM}}$ (M_\odot)	$\log \lambda_{\text{Edd}}$ [σ_l]	$\log \lambda_{\text{Edd}}$ [FWHM]
GB6J123431+645545	3.03	0.098	19.00	59	3499 ± 62	6193 ± 297	46.683 ± 0.006	44.743 ± 0.011	47.337 ± 0.006	9.24 ± 0.02	9.67 ± 0.04	-0.00 ± 0.02	-0.43 ± 0.04	
GB6J123505+362120	1.60	0.062	18.39	234	5216 ± 231	5419 ± 533	46.020 ± 0.011	44.460 ± 0.009	46.673 ± 0.011	9.24 ± 0.04	9.20 ± 0.09	-0.66 ± 0.04	-0.63 ± 0.09	
GB6J123605+242458	2.94	0.056	19.48	87	4044 ± 717	4645 ± 927	46.289 ± 0.009	44.737 ± 0.014	46.942 ± 0.009	9.16 ± 0.11	9.21 ± 0.27	-0.32 ± 0.11	-0.37 ± 0.27	
GB6J123736+192458	1.53	0.118	18.56	459	3417 ± 654	2129 ± 217	46.024 ± 0.011	44.798 ± 0.017	46.677 ± 0.011	8.87 ± 0.10	8.39 ± 0.09	-0.29 ± 0.10	0.19 ± 0.09	
GB6J124114+252408	3.06	0.056	19.00	49	5829 ± 1326	5032 ± 2886	46.675 ± 0.006	45.053 ± 0.043	47.328 ± 0.006	9.68 ± 0.13	9.48 ± 0.21	-0.45 ± 0.14	-0.25 ± 0.21	
GB6J124210+024112	3.18	0.098	19.97	56	4485 ± 238	6193 ± 354	46.245 ± 0.014	44.310 ± 0.013	46.898 ± 0.014	9.22 ± 0.04	9.43 ± 0.05	-0.43 ± 0.05	-0.64 ± 0.05	
GB6J124210+371944	3.82	0.065	19.37	372	4350 ± 223	2322 ± 285	46.476 ± 0.010	44.923 ± 0.011	47.129 ± 0.010	9.32 ± 0.04	8.70 ± 0.11	-0.29 ± 0.04	0.32 ± 0.11	
GB6J124708+274118	2.44	0.057	19.30	168	4209 ± 364	7548 ± 1510	46.224 ± 0.013	44.483 ± 0.013	46.877 ± 0.013	9.16 ± 0.06	9.59 ± 0.14	-0.38 ± 0.06	-0.82 ± 0.14	
GB6J125428+453607	1.65	0.088	18.66	151	4748 ± 296	6387 ± 355	46.135 ± 0.012	44.308 ± 0.012	46.789 ± 0.012	9.21 ± 0.05	9.40 ± 0.05	-0.53 ± 0.05	-0.71 ± 0.05	
GB6J125915+101633	3.00	0.080	19.94	56	3796 ± 225	2710 ± 279	46.023 ± 0.014	44.734 ± 0.010	46.677 ± 0.014	8.96 ± 0.05	8.60 ± 0.10	-0.38 ± 0.05	-0.02 ± 0.09	
GB6J130222+270911	3.43	0.040	19.36	68	4124 ± 117	5419 ± 517	46.254 ± 0.012	44.788 ± 0.009	46.907 ± 0.012	9.16 ± 0.03	9.32 ± 0.08	-0.35 ± 0.03	-0.52 ± 0.08	
GB6J130252+232245	3.19	0.080	19.11	60	3141 ± 92	2516 ± 411	46.495 ± 0.009	44.762 ± 0.011	47.148 ± 0.009	9.05 ± 0.03	8.78 ± 0.14	0.00 ± 0.03	0.26 ± 0.14	
GB6J130603+552947	1.60	0.078	18.24	249	4758 ± 154	4064 ± 269	46.211 ± 0.011	44.822 ± 0.009	46.864 ± 0.011	9.26 ± 0.03	9.05 ± 0.06	-0.49 ± 0.03	-0.29 ± 0.06	
GB6J130909+555731	1.63	0.074	17.72	423	3129 ± 52	6000 ± 339	46.601 ± 0.006	44.785 ± 0.008	47.254 ± 0.006	9.10 ± 0.02	9.59 ± 0.05	0.05 ± 0.01	-0.44 ± 0.05	
GB6J130942+404825	2.91	0.079	19.11	131	4150 ± 120	2903 ± 265	46.659 ± 0.005	44.912 ± 0.008	47.312 ± 0.005	9.38 ± 0.03	9.00 ± 0.08	-0.16 ± 0.02	0.22 ± 0.08	
GB6J131058+323339	1.64	0.059	18.81	870	2374 ± 127	3677 ± 872	46.330 ± 0.009	44.173 ± 0.014	46.983 ± 0.009	8.72 ± 0.05	9.03 ± 0.18	0.17 ± 0.05	-0.14 ± 0.18	
GB6J131341+102716	2.91	0.083	18.82	162	4789 ± 498	2903 ± 313	46.586 ± 0.007	45.096 ± 0.011	47.239 ± 0.007	9.46 ± 0.09	8.96 ± 0.10	-0.32 ± 0.09	0.18 ± 0.10	
GB6J131813+180657	2.08	0.087	19.44	131	3452 ± 93	2903 ± 413	45.927 ± 0.014	44.458 ± 0.011	46.581 ± 0.014	8.83 ± 0.03	8.61 ± 0.13	-0.35 ± 0.02	-0.13 ± 0.13	
GB6J131907+621725	3.07	0.108	19.19	144	5609 ± 1586	2322 ± 196	46.568 ± 0.007	45.099 ± 0.021	47.221 ± 0.007	9.59 ± 0.23	8.75 ± 0.08	-0.47 ± 0.23	0.37 ± 0.08	
GB6J132211+214803	1.68	0.088	18.80	182	4177 ± 442	2129 ± 273	46.088 ± 0.012	44.831 ± 0.012	46.741 ± 0.012	9.08 ± 0.10	8.42 ± 0.11	-0.44 ± 0.10	0.22 ± 0.11	
GB6J132254+391208	2.98	0.053	17.62	208	4960 ± 256	4838 ± 462	46.969 ± 0.004	45.551 ± 0.915	47.623 ± 0.004	9.69 ± 0.04	9.60 ± 0.13	-0.17 ± 0.04	-0.08 ± 0.18	
GB6J132512+112338	4.42	0.105	19.41	62	3463 ± 82	3484 ± 356	46.568 ± 0.008	45.208 ± 0.011	47.221 ± 0.008	9.17 ± 0.02	9.10 ± 0.10	-0.05 ± 0.02	0.02 ± 0.18	
GB6J132702+031258	2.83	0.094	18.97	80	3409 ± 136	3484 ± 431	46.391 ± 0.013	44.715 ± 0.018	47.044 ± 0.013	9.06 ± 0.04	9.01 ± 0.13	-0.12 ± 0.04	-0.07 ± 0.18	
GB6J132720+432629	2.09	0.070	19.21	576	4045 ± 135	3871 ± 608	45.979 ± 0.013	44.584 ± 0.011	46.632 ± 0.013	8.99 ± 0.03	8.88 ± 0.18	-0.46 ± 0.03	-0.35 ± 0.18	
GB6J132900+105259	1.94	0.112	18.87	112	5640 ± 657	4838 ± 529	45.954 ± 0.038	44.751 ± 0.013	46.607 ± 0.038	9.27 ± 0.09	9.07 ± 0.15	-0.76 ± 0.09	-0.56 ± 0.14	
GB6J133030+495431	2.87	0.048	18.77	110	4174 ± 133	6387 ± 498	46.608 ± 0.006	44.832 ± 0.008	47.261 ± 0.006	9.35 ± 0.03	9.65 ± 0.07	-0.19 ± 0.03	-0.49 ± 0.08	
GB6J133335+164838	2.08	0.085	16.12	615	4209 ± 85	5032 ± 306	47.541 ± 0.003	45.535 ± 0.007	48.194 ± 0.003	9.86 ± 0.02	9.94 ± 0.05	0.24 ± 0.02	0.15 ± 0.05	
GB6J133512+025311	1.86	0.096	17.77	144	4697 ± 149	2322 ± 268	46.580 ± 0.010	44.866 ± 0.009	47.234 ± 0.010	9.44 ± 0.03	8.76 ± 0.10	-0.31 ± 0.03	0.37 ± 0.10	
GB6J133825+250118	2.82	0.045	19.79	93	3680 ± 75	5032 ± 451	46.125 ± 0.011	44.427 ± 0.009	46.778 ± 0.011	8.99 ± 0.02	9.19 ± 0.08	-0.31 ± 0.02	-0.51 ± 0.08	
GB6J133923+632854	2.56	0.101	19.20	419	6825 ± 304	1935 ± 229	46.408 ± 0.006	45.029 ± 0.010	47.061 ± 0.006	9.67 ± 0.04	8.51 ± 0.10	-0.71 ± 0.04	0.45 ± 0.08	
GB6J134023+375458	3.11	0.039	18.44	260	5598 ± 304	2710 ± 313	46.751 ± 0.006	45.323 ± 0.009	47.405 ± 0.006	9.68 ± 0.05	8.98 ± 0.10	-0.38 ± 0.05	0.32 ± 0.10	
GB6J134222+511006	2.60	0.053	19.38	129	3998 ± 620	3677 ± 349	46.433 ± 0.008	44.763 ± 0.017	47.086 ± 0.008	9.22 ± 0.10	9.08 ± 0.08	-0.24 ± 0.10	-0.09 ± 0.08	
GB6J134723+183526	2.18	0.097	19.06	441	4312 ± 161	4838 ± 223	46.241 ± 0.010	44.590 ± 0.008	46.894 ± 0.010	9.19 ± 0.03	9.22 ± 0.04	-0.39 ± 0.04	-0.42 ± 0.04	
GB6J134811+193520	4.40	0.098	20.73	38	5359 ± 280	4838 ± 247	46.337 ± 0.013	44.609 ± 0.012	46.990 ± 0.013	9.43 ± 0.05	9.27 ± 0.05	-0.54 ± 0.05	-0.38 ± 0.04	
GB6J135257+021533	2.59	0.108	19.19	70	5278 ± 486	1935 ± 256	46.338 ± 0.009	44.718 ± 0.013	46.991 ± 0.009	9.41 ± 0.08	8.47 ± 0.12	-0.52 ± 0.09	0.42 ± 0.12	
GB6J135350+015154	1.61	0.110	18.68	227	4372 ± 164	3290 ± 570	45.962 ± 0.018	44.855 ± 0.008	46.615 ± 0.018	9.05 ± 0.03	8.73 ± 0.15	-0.54 ± 0.03	-0.22 ± 0.11	
GB6J135549+245307	2.69	0.075	19.27	60	6011 ± 180	4064 ± 477	46.281 ± 0.009	44.810 ± 0.009	46.935 ± 0.009	9.50 ± 0.03	9.09 ± 0.10	-0.66 ± 0.03	-0.25 ± 0.10	
GB6J140500+041544	3.21	0.112	19.30	1008	4777 ± 349	2710 ± 337	46.393 ± 0.019	45.135 ± 0.012	47.046 ± 0.019	9.36 ± 0.06	8.79 ± 0.12	-0.41 ± 0.06	0.15 ± 0.12	
GB6J140507+405655	2.01	0.071	19.28	267	5007 ± 157	5419 ± 536	45.924 ± 0.064	44.676 ± 0.008	46.577 ± 0.064	9.15 ± 0.04	9.15 ± 0.09	-0.67 ± 0.04	-0.67 ± 0.09	
GB6J140517+341856	2.90	0.066	19.31	138	3574 ± 152	5032 ± 192	46.152 ± 0.010	44.892 ± 0.009	46.805 ± 0.010	8.98 ± 0.04	9.20 ± 0.03	-0.27 ± 0.04	-0.50 ± 0.03	
GB6J140654+343328	2.56	0.067	18.71	204	2809 ± 68	3290 ± 318	46.573 ± 0.005	45.011 ± 0.010	47.227 ± 0.005	8.99 ± 0.02	9.06 ± 0.09	0.14 ± 0.02	0.07 ± 0.09	

Continued on next page

name	z	A_V	r-mag	$S_{5\text{GHz}}$ (mJy)	σ_l (km s $^{-1}$)	FWHM (km s $^{-1}$)	$\log \lambda L_{1350}$ (erg s $^{-1}$)	$\log L_{CIV}$ (erg s $^{-1}$)	$\log L_{\text{bol}}$ (erg s $^{-1}$)	$\log M_\sigma$ (M_\odot)	$\log M_{\text{FWHM}}$ (M_\odot)	$\log \lambda_{\text{Edd}}$ [σ_l]	$\log \lambda_{\text{Edd}}$ [FWHM]
GB6J140812+561327	2.02	0.063	18.62	309	2431 ± 75	5419 ± 182	46.406 ± 0.023	44.337 ± 0.012	47.060 ± 0.023	8.78 ± 0.03	9.40 ± 0.03	0.18 ± 0.03	-0.44 ± 0.03
GB6J141031+614138	2.25	0.092	18.80	127	4230 ± 108	5226 ± 398	46.389 ± 0.009	44.690 ± 0.010	47.042 ± 0.009	9.25 ± 0.02	9.36 ± 0.07	-0.31 ± 0.02	-0.42 ± 0.04
GB6J141107+003604	1.72	0.162	18.45	205	-	-	-	-	-	-	-	-	-
GB6J141152+430022	3.22	0.051	20.14	109	4939 ± 342	3484 ± 182	46.051 ± 0.020	44.493 ± 0.015	46.704 ± 0.020	9.20 ± 0.06	8.83 ± 0.05	-0.60 ± 0.06	-0.23 ± 0.05
GB6J141155+341516	1.82	0.075	18.36	147	3713 ± 177	2710 ± 396	46.255 ± 0.010	44.954 ± 0.010	46.908 ± 0.010	9.06 ± 0.04	8.72 ± 0.13	-0.26 ± 0.04	0.09 ± 0.14
GB6J141203+125716	2.43	0.085	19.48	109	2471 ± 130	2516 ± 266	45.957 ± 0.017	44.559 ± 0.010	46.610 ± 0.017	8.55 ± 0.05	8.50 ± 0.10	-0.04 ± 0.05	0.01 ± 0.10
GB6J141212+062408	4.47	0.110	20.23	34	3052 ± 313	7161 ± 749	46.494 ± 0.015	44.252 ± 0.020	47.147 ± 0.015	9.02 ± 0.08	9.69 ± 0.09	0.03 ± 0.08	-0.65 ± 0.09
GB6J141319+450527	3.11	0.036	19.28	150	1902 ± 134	3290 ± 373	46.416 ± 0.017	44.674 ± 0.013	47.069 ± 0.017	8.57 ± 0.05	8.98 ± 0.10	0.40 ± 0.06	-0.01 ± 0.10
GB6J141528+370619	2.37	0.043	17.62	381	5048 ± 147	6774 ± 329	46.746 ± 0.005	45.236 ± 0.008	47.399 ± 0.005	9.59 ± 0.03	9.78 ± 0.04	-0.29 ± 0.03	-0.48 ± 0.04
GB6J141708+460659	1.55	0.041	17.62	797	3979 ± 306	3290 ± 415	46.705 ± 0.004	45.115 ± 0.011	47.358 ± 0.004	9.36 ± 0.07	9.13 ± 0.11	-0.11 ± 0.06	0.13 ± 0.11
GB6J141918+075926	3.05	0.118	19.76	58	1780 ± 41	3871 ± 400	46.303 ± 0.010	44.116 ± 0.016	46.956 ± 0.010	8.45 ± 0.02	9.06 ± 0.09	0.40 ± 0.02	-0.20 ± 0.08
GB6J142037+471431	3.24	0.068	19.39	45	5153 ± 711	2129 ± 236	46.424 ± 0.010	44.967 ± 0.017	47.077 ± 0.010	9.44 ± 0.14	8.60 ± 0.10	-0.46 ± 0.13	0.38 ± 0.10
GB6J142122+464551	1.67	0.058	18.08	223	4249 ± 197	6000 ± 376	46.302 ± 0.011	44.600 ± 0.011	46.955 ± 0.011	9.21 ± 0.04	9.44 ± 0.05	-0.35 ± 0.04	-0.58 ± 0.05
GB6J142330+120005	1.61	0.093	17.88	571	4013 ± 509	2129 ± 300	46.364 ± 0.007	44.993 ± 0.013	47.017 ± 0.007	9.19 ± 0.10	8.57 ± 0.12	-0.27 ± 0.10	0.35 ± 0.12
GB6J142436+225551	3.62	0.179	15.41	548	-	-	-	-	-	-	-	-	-
GB6J142822+563601	2.13	0.068	19.20	88	4671 ± 469	5226 ± 524	46.134 ± 0.028	44.674 ± 0.013	46.787 ± 0.028	9.20 ± 0.09	9.23 ± 0.09	-0.51 ± 0.09	-0.54 ± 0.10
GB6J142921+540613	3.01	0.057	19.91	716	3675 ± 105	4645 ± 590	46.110 ± 0.012	44.338 ± 0.013	46.763 ± 0.012	8.98 ± 0.03	9.11 ± 0.12	-0.32 ± 0.03	-0.45 ± 0.12
GB6J143009+104340	1.71	0.110	18.52	1194	3717 ± 166	5419 ± 333	46.337 ± 0.008	44.519 ± 0.012	46.990 ± 0.008	9.11 ± 0.04	9.37 ± 0.06	-0.22 ± 0.04	-0.48 ± 0.06
GB6J143023+420450	4.71	0.058	21.00	337	3541 ± 186	8129 ± 450	46.627 ± 0.011	44.602 ± 0.014	47.280 ± 0.011	9.22 ± 0.05	9.87 ± 0.05	-0.04 ± 0.05	-0.69 ± 0.05
GB6J143533+543605	3.81	0.062	20.05	86	3077 ± 91	2322 ± 305	46.112 ± 0.017	44.734 ± 0.011	46.766 ± 0.017	8.83 ± 0.03	8.51 ± 0.12	-0.16 ± 0.03	0.15 ± 0.12
GB6J143646+633645	2.07	0.071	16.99	757	3890 ± 85	3677 ± 357	46.997 ± 0.005	45.387 ± 0.008	47.650 ± 0.005	9.50 ± 0.02	9.38 ± 0.09	0.05 ± 0.02	0.17 ± 0.09
GB6J143708+040536	2.02	0.139	18.19	127	3862 ± 183	2322 ± 295	46.618 ± 0.008	45.067 ± 0.009	47.271 ± 0.008	9.29 ± 0.04	8.78 ± 0.12	-0.12 ± 0.04	0.39 ± 0.12
GB6J143721+511259	2.16	0.055	19.56	117	2879 ± 347	5226 ± 372	46.132 ± 0.012	44.243 ± 0.011	46.785 ± 0.012	8.78 ± 0.08	9.23 ± 0.06	-0.09 ± 0.08	-0.54 ± 0.06
GB6J143828+441811	2.10	0.076	19.30	265	2635 ± 89	6000 ± 225	46.108 ± 0.032	44.355 ± 0.010	46.761 ± 0.032	8.69 ± 0.03	9.33 ± 0.04	-0.03 ± 0.03	-0.67 ± 0.04
GB6J143911+111749	2.59	0.084	18.47	133	3771 ± 169	2903 ± 406	46.448 ± 0.006	45.019 ± 0.009	47.101 ± 0.006	9.18 ± 0.04	8.88 ± 0.12	-0.18 ± 0.04	0.12 ± 0.12
GB6J144349+564553	2.76	0.070	19.69	66	3244 ± 142	5032 ± 424	46.344 ± 0.011	44.707 ± 0.010	46.997 ± 0.011	8.99 ± 0.04	9.31 ± 0.08	-0.10 ± 0.04	-0.41 ± 0.08
GB6J144754+582435	2.98	0.056	18.28	55	2184 ± 206	1355 ± 236	46.775 ± 0.005	44.828 ± 0.013	47.428 ± 0.005	8.88 ± 0.08	8.39 ± 0.15	0.45 ± 0.08	0.93 ± 0.15
GB6J145031+091012	2.61	0.110	19.72	378	3734 ± 350	2129 ± 330	46.116 ± 0.013	44.353 ± 0.015	46.769 ± 0.013	9.00 ± 0.08	8.44 ± 0.14	-0.33 ± 0.08	0.23 ± 0.14
GB6J145300+103606	2.27	0.096	19.31	111	3850 ± 124	5806 ± 397	46.161 ± 0.011	44.704 ± 0.009	46.815 ± 0.011	9.05 ± 0.03	9.33 ± 0.06	-0.33 ± 0.03	-0.62 ± 0.06
GB6J145553+443129	2.69	0.095	19.45	192	2978 ± 167	1935 ± 185	46.060 ± 0.014	44.574 ± 0.012	46.714 ± 0.014	8.77 ± 0.05	8.33 ± 0.08	-0.16 ± 0.05	0.29 ± 0.08
GB6J145721+051915	3.18	0.164	19.03	77	4326 ± 119	7742 ± 398	46.688 ± 0.006	44.890 ± 0.010	47.341 ± 0.006	9.43 ± 0.02	9.86 ± 0.05	-0.19 ± 0.02	-0.62 ± 0.05
GB6J145738+373000	3.85	0.061	20.73	45	3468 ± 91	4064 ± 995	46.042 ± 0.026	44.552 ± 0.013	46.695 ± 0.026	8.89 ± 0.03	8.96 ± 0.43	-0.30 ± 0.03	-0.37 ± 0.43
GB6J145936+444152	3.40	0.091	20.28	164	3611 ± 62	7161 ± 264	46.367 ± 0.016	44.543 ± 0.011	47.020 ± 0.016	9.10 ± 0.02	9.62 ± 0.03	-0.18 ± 0.02	-0.70 ± 0.03
GB6J150328+041959	3.66	0.203	18.09	147	4652 ± 178	3871 ± 522	47.159 ± 0.004	45.240 ± 0.009	47.812 ± 0.004	9.74 ± 0.03	9.51 ± 0.13	-0.03 ± 0.03	0.20 ± 0.13
GB6J150424+102943	1.84	0.121	18.22	2325	3271 ± 285	3097 ± 338	46.140 ± 0.019	44.619 ± 0.012	46.793 ± 0.019	8.89 ± 0.07	8.78 ± 0.10	-0.20 ± 0.07	-0.08 ± 0.10
GB6J150759+041518	1.70	0.203	18.21	240	3901 ± 122	6580 ± 519	46.401 ± 0.008	44.710 ± 0.010	47.054 ± 0.008	9.18 ± 0.03	9.57 ± 0.07	-0.23 ± 0.03	-0.62 ± 0.07
GB6J150805+185232	1.83	0.141	18.50	243	2924 ± 59	5806 ± 246	46.398 ± 0.008	44.490 ± 0.009	47.051 ± 0.008	8.93 ± 0.02	9.46 ± 0.03	0.02 ± 0.02	-0.51 ± 0.04
GB6J150824+334706	2.21	0.073	18.35	115	2918 ± 93	3677 ± 483	46.332 ± 0.011	44.635 ± 0.009	46.985 ± 0.011	8.90 ± 0.03	9.03 ± 0.11	-0.01 ± 0.03	-0.14 ± 0.12
GB6J151002+570256	4.31	0.078	20.34	292	2540 ± 113	2322 ± 272	46.532 ± 0.010	44.830 ± 0.014	47.185 ± 0.010	8.88 ± 0.04	8.73 ± 0.11	0.20 ± 0.04	0.35 ± 0.11
GB6J151509+213326	2.25	0.216	18.32	89	4063 ± 62	2710 ± 453	46.617 ± 0.005	45.033 ± 0.010	47.270 ± 0.005	9.33 ± 0.01	8.91 ± 0.14	-0.16 ± 0.01	0.26 ± 0.15
GB6J151618+052445	1.71	0.197	18.66	181	4288 ± 281	2903 ± 228	46.307 ± 0.009	44.703 ± 0.011	46.960 ± 0.009	9.22 ± 0.06	8.81 ± 0.07	-0.36 ± 0.06	0.05 ± 0.07

Continued on next page

	name	z	A_V	r-mag	$S_{5\text{GHz}}$ (mJy)	σ_l (km s $^{-1}$)	FWHM (km s $^{-1}$)	$\log \lambda L_{1350}$ (erg s $^{-1}$)	$\log L_{CIV}$ (erg s $^{-1}$)	$\log L_{\text{bol}}$ (erg s $^{-1}$)	$\log M_\sigma$ (M_\odot)	$\log M_{\text{FWHM}}$ (M_\odot)	$\log \lambda_{\text{Edd}}$ [σ_l]	$\log \lambda_{\text{Edd}}$ [FWHM]
GB6J152044+473253	2.81	0.114	18.53	86	3918 ± 146	2516 ± 225	46.564 ± 0.006	45.172 ± 0.010	47.217 ± 0.006	9.27 ± 0.03	8.82 ± 0.08	-0.16 ± 0.03	0.30 ± 0.08	
GB6J152118+175605	3.06	0.212	19.11	208	5451 ± 200	2322 ± 347	46.427 ± 0.008	45.238 ± 0.008	47.080 ± 0.008	9.49 ± 0.03	8.68 ± 0.13	-0.51 ± 0.03	0.30 ± 0.13	
GB6J152141+051650	2.53	0.194	18.88	67	4163 ± 262	2710 ± 339	46.570 ± 0.006	45.095 ± 0.010	47.224 ± 0.006	9.33 ± 0.05	8.89 ± 0.11	-0.21 ± 0.05	0.24 ± 0.11	
GB6J152149+433636	2.17	0.102	18.89	220	2637 ± 64	2516 ± 332	46.392 ± 0.009	44.720 ± 0.011	47.045 ± 0.009	8.84 ± 0.02	8.73 ± 0.11	0.10 ± 0.02	0.22 ± 0.11	
GB6J152642+665057	3.02	0.142	17.86	404	-	-	-	-	-	-	-	-	-	
GB6J153324+070516	2.96	0.219	20.02	82	3046 ± 69	6967 ± 183	45.908 ± 0.018	44.197 ± 0.009	46.561 ± 0.018	8.71 ± 0.02	9.36 ± 0.02	-0.25 ± 0.02	-0.90 ± 0.02	
GB6J153456+583920	1.90	0.086	18.24	119	2756 ± 252	4451 ± 315	46.378 ± 0.018	44.772 ± 0.011	47.031 ± 0.018	8.87 ± 0.08	9.22 ± 0.06	0.06 ± 0.08	-0.29 ± 0.06	
GB6J153515+483709	2.56	0.072	17.84	163	4008 ± 58	5806 ± 288	46.862 ± 0.004	44.959 ± 0.007	47.515 ± 0.004	9.45 ± 0.01	9.70 ± 0.04	-0.04 ± 0.01	-0.29 ± 0.04	
GB6J153533+025419	4.39	0.213	20.59	53	3461 ± 219	7935 ± 528	46.363 ± 0.013	44.363 ± 0.017	47.016 ± 0.013	9.06 ± 0.05	9.71 ± 0.06	-0.15 ± 0.06	-0.80 ± 0.06	
GB6J153622+020204	2.99	0.249	19.28	53	6697 ± 1095	2129 ± 214	46.369 ± 0.007	45.111 ± 0.020	47.022 ± 0.007	9.64 ± 0.16	8.57 ± 0.09	-0.72 ± 0.16	0.35 ± 0.09	
GB6J153753+085026	2.22	0.169	18.65	101	4082 ± 143	5226 ± 825	46.388 ± 0.005	44.597 ± 0.018	47.041 ± 0.005	9.22 ± 0.03	9.36 ± 0.29	-0.28 ± 0.03	-0.42 ± 0.29	
GB6J153926+160406	2.53	0.155	19.21	336	4084 ± 94	5613 ± 333	46.474 ± 0.005	44.542 ± 0.011	47.128 ± 0.005	9.26 ± 0.02	9.47 ± 0.05	-0.24 ± 0.02	-0.44 ± 0.05	
GB6J153938+274433	2.20	0.155	18.28	212	2280 ± 273	2903 ± 378	44.830 ± 0.113	43.685 ± 0.015	45.483 ± 0.113	7.89 ± 0.12	8.03 ± 0.13	-0.50 ± 0.10	-0.64 ± 0.12	
GB6J154125+534827	2.55	0.068	18.93	248	5379 ± 246	2516 ± 336	46.575 ± 0.007	45.072 ± 0.009	47.228 ± 0.007	9.56 ± 0.04	8.83 ± 0.12	-0.43 ± 0.04	0.30 ± 0.12	
GB6J154503+513502	1.93	0.059	17.57	588	4140 ± 106	5613 ± 429	46.820 ± 0.008	44.975 ± 0.007	47.473 ± 0.008	9.46 ± 0.02	9.65 ± 0.07	-0.09 ± 0.02	-0.28 ± 0.07	
GB6J154534+200654	2.13	0.228	19.13	125	3067 ± 238	4258 ± 448	46.235 ± 0.017	44.519 ± 0.014	46.888 ± 0.017	8.89 ± 0.07	9.10 ± 0.10	-0.10 ± 0.07	-0.32 ± 0.10	
GB6J154827+073819	2.89	0.150	19.29	81	3840 ± 94	4645 ± 359	46.291 ± 0.012	44.732 ± 0.009	46.944 ± 0.012	9.11 ± 0.02	9.21 ± 0.07	-0.27 ± 0.02	-0.36 ± 0.07	
GB6J154912+035217	3.94	0.364	20.78	51	1951 ± 78	2322 ± 722	45.985 ± 0.026	44.534 ± 0.021	46.638 ± 0.026	8.36 ± 0.03	8.44 ± 0.37	0.18 ± 0.04	0.09 ± 0.37	
GB6J154917+503810	2.17	0.067	18.53	731	5349 ± 726	2710 ± 386	46.372 ± 0.008	44.886 ± 0.019	47.025 ± 0.008	9.44 ± 0.10	8.78 ± 0.12	-0.52 ± 0.10	0.14 ± 0.12	
GB6J154945+613415	2.27	0.059	19.04	121	6659 ± 332	7548 ± 516	46.187 ± 0.012	44.757 ± 0.011	46.840 ± 0.012	9.54 ± 0.04	9.57 ± 0.06	-0.80 ± 0.04	-0.84 ± 0.06	
GB6J155538+110648	2.66	0.209	18.95	149	5387 ± 456	3484 ± 420	46.351 ± 0.006	44.823 ± 0.010	47.004 ± 0.006	9.44 ± 0.07	8.99 ± 0.12	-0.54 ± 0.07	-0.09 ± 0.11	
GB6J155930+030444	3.89	0.407	20.01	414	2366 ± 195	2129 ± 314	46.515 ± 0.008	45.042 ± 0.017	47.168 ± 0.008	8.81 ± 0.06	8.65 ± 0.12	0.26 ± 0.06	0.42 ± 0.11	
GB6J155948+080524	2.18	0.191	17.40	114	4063 ± 83	7161 ± 367	47.034 ± 0.004	45.037 ± 0.008	47.687 ± 0.004	9.56 ± 0.02	9.98 ± 0.04	0.03 ± 0.02	-0.39 ± 0.04	
GB6J160017+183828	2.40	0.171	18.77	154	3301 ± 217	4064 ± 289	46.405 ± 0.005	44.966 ± 0.008	47.058 ± 0.005	9.04 ± 0.05	9.15 ± 0.06	-0.08 ± 0.05	-0.19 ± 0.06	
GB6J160103+170658	2.61	0.180	19.69	83	4569 ± 386	2322 ± 498	46.082 ± 0.012	44.924 ± 0.026	46.735 ± 0.012	9.15 ± 0.08	8.50 ± 0.23	-0.52 ± 0.08	0.14 ± 0.29	
GB6J160154+135703	2.24	0.228	18.38	365	3965 ± 557	2903 ± 347	46.464 ± 0.011	44.924 ± 0.013	47.117 ± 0.011	9.23 ± 0.11	8.89 ± 0.11	-0.22 ± 0.11	0.13 ± 0.11	
GB6J160214+241832	1.79	0.296	17.89	214	4000 ± 99	3484 ± 406	46.533 ± 0.007	44.604 ± 0.008	47.186 ± 0.007	9.28 ± 0.02	9.09 ± 0.10	-0.19 ± 0.02	-0.00 ± 0.10	
GB6J160357+573101	2.85	0.103	17.33	365	5272 ± 411	3871 ± 255	47.296 ± 0.003	45.449 ± 0.009	47.949 ± 0.003	9.92 ± 0.06	9.58 ± 0.06	-0.07 ± 0.06	0.27 ± 0.06	
GB6J160524+303836	2.69	0.140	19.40	75	3533 ± 561	2322 ± 355	46.185 ± 0.010	44.772 ± 0.015	46.838 ± 0.010	8.98 ± 0.13	8.55 ± 0.14	-0.25 ± 0.13	0.19 ± 0.14	
GB6J160820+561407	1.95	0.056	18.22	236	4413 ± 152	4258 ± 324	46.635 ± 0.007	44.883 ± 0.008	47.289 ± 0.007	9.42 ± 0.03	9.32 ± 0.07	-0.23 ± 0.03	-0.13 ± 0.07	
GB6J161004+181156	3.12	0.201	18.27	131	4823 ± 136	7354 ± 395	46.766 ± 0.004	44.921 ± 0.007	47.419 ± 0.004	9.56 ± 0.02	9.86 ± 0.05	-0.24 ± 0.02	-0.54 ± 0.05	
GB6J161252+275841	3.54	0.207	19.81	60	4677 ± 160	2710 ± 283	46.346 ± 0.012	44.835 ± 0.009	46.999 ± 0.012	9.31 ± 0.03	8.77 ± 0.09	-0.41 ± 0.03	0.13 ± 0.09	
GB6J161428+174216	2.81	0.222	19.84	72	3436 ± 231	3677 ± 337	46.157 ± 0.013	44.848 ± 0.010	46.810 ± 0.013	8.95 ± 0.05	8.93 ± 0.08	-0.24 ± 0.05	-0.22 ± 0.08	
GB6J161446+253622	2.45	0.236	18.89	90	3618 ± 142	5806 ± 407	46.170 ± 0.010	44.694 ± 0.009	46.823 ± 0.010	9.00 ± 0.03	9.34 ± 0.06	-0.27 ± 0.03	-0.62 ± 0.06	
GB6J161526+431255	3.14	0.053	19.80	129	5223 ± 336	5613 ± 381	46.081 ± 0.015	44.583 ± 0.011	46.734 ± 0.015	9.27 ± 0.06	9.26 ± 0.06	-0.63 ± 0.06	-0.63 ± 0.06	
GB6J161630+142910	2.98	0.199	20.04	58	3271 ± 111	5419 ± 552	46.222 ± 0.012	44.796 ± 0.010	46.875 ± 0.012	8.94 ± 0.03	9.31 ± 0.09	-0.16 ± 0.03	-0.53 ± 0.03	
GB6J161638+045924	3.22	0.291	19.26	916	-	-	-	-	-	-	-	-	-	
GB6J161656+362145	2.27	0.060	18.50	286	3310 ± 124	3871 ± 434	46.398 ± 0.008	44.974 ± 0.009	47.051 ± 0.008	9.04 ± 0.03	9.11 ± 0.10	-0.09 ± 0.03	-0.16 ± 0.16	
GB6J161904+061257	2.10	0.236	19.06	971	4343 ± 187	2710 ± 510	46.291 ± 0.021	44.809 ± 0.010	46.944 ± 0.021	9.22 ± 0.04	8.74 ± 0.19	-0.38 ± 0.04	0.10 ± 0.15	
GB6J161941+525617	2.35	0.084	16.74	128	4071 ± 72	4838 ± 426	47.199 ± 0.003	45.532 ± 0.007	47.852 ± 0.003	9.65 ± 0.02	9.73 ± 0.07	0.11 ± 0.02	0.03 ± 0.07	
GB6J162030+490149	1.51	0.058	18.49	442	2718 ± 90	3097 ± 576	46.271 ± 0.006	44.574 ± 0.011	46.924 ± 0.006	8.80 ± 0.03	8.85 ± 0.13	0.02 ± 0.03	-0.02 ± 0.12	

Continued on next page

The evolution of the heaviest SMBHs in jetted AGNs

name	z	A_V	r-mag	$S_{5\text{GHz}}$ (mJy)	σ_l (km s $^{-1}$)	FWHM (km s $^{-1}$)	$\text{Log } \lambda L_{1350}$ (erg s $^{-1}$)	$\text{Log } L_{CIV}$ (erg s $^{-1}$)	$\text{Log } L_{\text{bol}}$ (erg s $^{-1}$)	$\text{Log } M_\sigma$ (M_\odot)	$\text{Log } M_{\text{FWHM}}$ (M_\odot)	$\text{Log } \lambda_{\text{Edd}}$ [σ_l]	$\text{Log } \lambda_{\text{Edd}}$ [FWHM]
GB6J162308+390946	1.98	0.042	16.84	244	3981 ± 633	4451 ± 344	46.906 ± 0.005	45.280 ± 0.010	47.559 ± 0.005	9.47 ± 0.09	9.50 ± 0.07	-0.01 ± 0.09	-0.04 ± 0.07
GB6J162956+095959	5.00	0.283	21.97	33	2436 ± 779	5613 ± 1819	46.314 ± 0.151	44.079 ± 0.114	46.967 ± 0.151	8.73 ± 0.32	9.38 ± 0.33	0.14 ± 0.32	-0.52 ± 0.34
GB6J163355+153446	2.44	0.273	19.59	99	4923 ± 308	5419 ± 372	46.307 ± 0.006	44.491 ± 0.011	46.960 ± 0.006	9.34 ± 0.05	9.35 ± 0.07	-0.48 ± 0.05	-0.49 ± 0.06
GB6J163412+320339	2.33	0.097	17.46	248	4858 ± 143	5613 ± 1031	46.899 ± 0.004	45.413 ± 0.019	47.553 ± 0.004	9.64 ± 0.03	9.69 ± 0.33	-0.19 ± 0.03	-0.24 ± 0.33
GB6J163515+380813	1.81	0.055	17.64	3221	3134 ± 160	3097 ± 347	46.578 ± 0.011	44.891 ± 0.008	47.232 ± 0.011	9.09 ± 0.04	9.01 ± 0.10	0.04 ± 0.04	0.12 ± 0.14
GB6J163731+195037	1.96	0.321	18.97	120	3000 ± 94	3290 ± 377	46.091 ± 0.032	44.863 ± 0.012	46.745 ± 0.032	8.79 ± 0.03	8.80 ± 0.11	-0.15 ± 0.03	-0.16 ± 0.11
GB6J164124+225714	2.06	0.224	18.94	446	2447 ± 98	4451 ± 2298	46.286 ± 0.016	44.256 ± 0.012	46.939 ± 0.016	8.72 ± 0.03	9.17 ± 0.27	0.12 ± 0.03	-0.33 ± 0.27
GB6J164148+334515	2.75	0.084	19.03	67	3438 ± 150	2516 ± 320	46.418 ± 0.024	44.989 ± 0.012	47.071 ± 0.024	9.08 ± 0.04	8.74 ± 0.11	-0.11 ± 0.04	0.23 ± 0.12
GB6J164157+511603	2.62	0.096	18.62	114	3939 ± 103	4064 ± 606	46.352 ± 0.009	45.001 ± 0.009	47.005 ± 0.009	9.17 ± 0.02	9.12 ± 0.14	-0.26 ± 0.02	-0.22 ± 0.14
GB6J164239+252316	1.73	0.210	18.30	515	3050 ± 97	6000 ± 322	46.495 ± 0.007	44.520 ± 0.010	47.148 ± 0.007	9.02 ± 0.03	9.54 ± 0.05	0.03 ± 0.03	-0.49 ± 0.05
GB6J164327+410359	3.86	0.050	20.11	38	2507 ± 76	1548 ± 212	46.211 ± 0.017	44.804 ± 0.010	46.864 ± 0.017	8.70 ± 0.03	8.21 ± 0.12	0.06 ± 0.03	0.55 ± 0.12
GB6J164856+460341	5.36	0.000	20.31	36	2604 ± 207	4645 ± 2100	46.260 ± 0.142	44.601 ± 0.045	46.913 ± 0.142	8.76 ± 0.11	9.19 ± 0.73	0.05 ± 0.10	-0.38 ± 0.71
GB6J165543+194846	3.26	0.348	19.85	169	3809 ± 185	3290 ± 214	46.317 ± 0.010	44.633 ± 0.009	46.970 ± 0.010	9.12 ± 0.04	8.92 ± 0.06	-0.25 ± 0.04	-0.05 ± 0.06
GB6J165634+182624	2.55	0.366	20.09	349	3713 ± 104	4451 ± 392	46.224 ± 0.008	44.971 ± 0.009	46.877 ± 0.008	9.05 ± 0.02	9.14 ± 0.08	-0.27 ± 0.03	-0.36 ± 0.08
GB6J165801+344330	1.94	0.082	17.99	474	4844 ± 283	2516 ± 269	46.519 ± 0.007	45.141 ± 0.011	47.172 ± 0.007	9.44 ± 0.05	8.80 ± 0.10	-0.36 ± 0.05	0.28 ± 0.10
GB6J165802+473749	1.61	0.088	17.75	1244	3729 ± 179	5226 ± 272	46.614 ± 0.004	44.798 ± 0.009	47.267 ± 0.004	9.26 ± 0.04	9.48 ± 0.05	-0.09 ± 0.04	-0.31 ± 0.05
GB6J165913+171418	2.01	0.351	18.90	142	3189 ± 109	5032 ± 249	46.471 ± 0.015	44.742 ± 0.014	47.124 ± 0.015	9.05 ± 0.03	9.37 ± 0.04	-0.02 ± 0.03	-0.35 ± 0.04
GB6J170732+112206	2.41	0.321	19.75	117	-	-	-	-	-	-	-	-	-
GB6J171103+383016	4.00	0.221	20.52	36	2188 ± 126	2129 ± 216	46.280 ± 0.015	44.542 ± 0.014	46.933 ± 0.015	8.62 ± 0.05	8.52 ± 0.10	0.21 ± 0.05	0.31 ± 0.10
GB6J172241+610604	2.06	0.130	19.13	245	-	-	-	-	-	-	-	-	-
GB6J172253+245836	2.25	0.305	18.11	378	4095 ± 117	5806 ± 400	46.836 ± 0.003	44.887 ± 0.008	47.489 ± 0.003	9.46 ± 0.03	9.69 ± 0.06	-0.07 ± 0.02	-0.30 ± 0.06
GB6J173928+495502	1.54	0.135	18.16	428	-	-	-	-	-	-	-	-	-
GB6J174006+450700	2.79	0.138	17.92	192	-	-	-	-	-	-	-	-	-
GB6J174048+434825	2.25	0.151	19.20	196	-	-	-	-	-	-	-	-	-
GB6J174614+622700	3.89	0.166	19.01	589	-	-	-	-	-	-	-	-	-
GB6J175602+574859	2.11	0.212	18.50	463	-	-	-	-	-	-	-	-	-
GB6J180024+384834	2.09	0.147	17.54	735	-	-	-	-	-	-	-	-	-
GB6J205332+010307	3.59	0.471	19.79	58	1290 ± 226	2903 ± 554	46.704 ± 0.098	44.910 ± 0.042	47.357 ± 0.098	8.38 ± 0.16	9.02 ± 0.17	0.87 ± 0.16	0.24 ± 0.17
GB6J210627+023120	2.94	0.420	18.94	131	-	-	-	-	-	-	-	-	-
GB6J212026+044746	3.15	0.494	19.61	66	3531 ± 102	2322 ± 218	46.415 ± 0.006	45.039 ± 0.008	47.068 ± 0.006	9.11 ± 0.02	8.67 ± 0.08	-0.14 ± 0.03	0.30 ± 0.08
GB6J212344+053534	1.94	0.377	17.44	2784	-	-	-	-	-	-	-	-	-
GB6J213638+004149	1.94	0.266	16.84	10938	6243 ± 385	4064 ± 482	47.064 ± 0.005	45.485 ± 0.009	47.717 ± 0.005	9.94 ± 0.05	9.50 ± 0.11	-0.33 ± 0.05	0.11 ± 0.11
GB6J213729+045109	2.37	0.265	19.86	143	2948 ± 71	6000 ± 227	46.129 ± 0.010	44.309 ± 0.010	46.782 ± 0.010	8.80 ± 0.02	9.34 ± 0.03	-0.12 ± 0.02	-0.66 ± 0.03
GB6J214755+083010	2.60	0.267	18.48	351	5117 ± 189	3290 ± 321	46.654 ± 0.004	44.942 ± 0.008	47.307 ± 0.004	9.55 ± 0.03	9.10 ± 0.09	-0.35 ± 0.03	0.11 ± 0.08
GB6J215304+124102	2.22	0.415	19.47	290	3710 ± 329	4838 ± 336	46.279 ± 0.014	44.491 ± 0.014	46.932 ± 0.014	9.08 ± 0.08	9.24 ± 0.07	-0.24 ± 0.08	-0.41 ± 0.07
GB6J215633+194734	2.47	0.381	18.48	77	3865 ± 1043	3677 ± 410	46.611 ± 0.004	45.287 ± 0.641	47.264 ± 0.004	9.29 ± 0.15	9.17 ± 0.10	-0.12 ± 0.15	-0.01 ± 0.10
GB6J215941+062832	2.72	0.266	19.39	68	4366 ± 139	4645 ± 383	46.414 ± 0.008	44.765 ± 0.009	47.067 ± 0.008	9.29 ± 0.03	9.27 ± 0.07	-0.32 ± 0.03	-0.31 ± 0.07
GB6J221747+022011	3.57	0.234	20.52	513	3309 ± 113	3290 ± 374	46.190 ± 0.016	44.587 ± 0.013	46.843 ± 0.016	8.93 ± 0.03	8.86 ± 0.20	-0.19 ± 0.03	-0.11 ± 0.20
GB6J221811+152042	2.33	0.257	18.64	183	-	-	-	-	-	-	-	-	-
GB6J221931+022955	2.22	0.260	18.71	124	4077 ± 58	5419 ± 509	46.378 ± 0.008	44.839 ± 0.009	47.031 ± 0.008	9.21 ± 0.01	9.39 ± 0.09	-0.28 ± 0.01	-0.46 ± 0.09
GB6J222307+145355	2.78	0.229	18.55	106	3887 ± 352	6387 ± 494	46.816 ± 0.003	45.057 ± 0.017	47.469 ± 0.003	9.40 ± 0.07	9.76 ± 0.07	-0.03 ± 0.07	-0.39 ± 0.07

Continued on next page

	name	z	A_V	r-mag	$S_{5\text{GHz}}$ (mJy)	σ_l (km s $^{-1}$)	FWHM (km s $^{-1}$)	Log λL_{1350} (erg s $^{-1}$)	Log L_{CIV} (erg s $^{-1}$)	Log L_{bol} (erg s $^{-1}$)	Log M_σ (M_\odot)	Log M_{FWHM} (M_\odot)	Log λ_{Edd} [σ_l]	Log λ_{Edd} [FWHM]
GB6J222537+211817	1.96	0.217	17.82	1024	2992 ± 68	5613 ± 273	46.907 ± 0.004	44.929 ± 0.010	47.560 ± 0.004	9.22 ± 0.02	9.70 ± 0.04	0.24 ± 0.02	-0.24 ± 0.04	
GB6J223307+161714	3.35	0.343	20.06	52	2581 ± 63	5032 ± 290	46.443 ± 0.009	44.528 ± 0.010	47.097 ± 0.009	8.85 ± 0.02	9.36 ± 0.05	0.15 ± 0.02	-0.36 ± 0.05	
GB6J223927+225959	2.93	0.228	18.29	78	2183 ± 51	1935 ± 222	46.902 ± 0.004	45.320 ± 0.012	47.555 ± 0.004	8.95 ± 0.02	8.77 ± 0.11	0.51 ± 0.02	0.68 ± 0.11	
GB6J224150+095356	1.71	0.327	18.62	675	-	-	-	-	-	-	-	-	-	
GB6J224352+190443	3.45	0.316	20.22	47	3831 ± 95	4645 ± 237	46.079 ± 0.018	44.283 ± 0.015	46.732 ± 0.018	9.00 ± 0.02	9.10 ± 0.04	-0.37 ± 0.02	-0.46 ± 0.05	
GB6J224434+260014	2.04	0.326	18.68	263	4073 ± 130	4451 ± 392	46.441 ± 0.006	45.067 ± 0.007	47.094 ± 0.006	9.24 ± 0.03	9.25 ± 0.08	-0.25 ± 0.03	-0.26 ± 0.08	
GB6J225153+221724	3.67	0.312	19.55	179	3559 ± 199	4838 ± 284	46.184 ± 0.017	44.431 ± 0.013	46.837 ± 0.017	8.99 ± 0.05	9.19 ± 0.05	-0.25 ± 0.05	-0.45 ± 0.05	
GB6J225717+024311	2.08	0.325	17.90	503	4304 ± 160	2903 ± 260	46.763 ± 0.004	45.086 ± 0.009	47.416 ± 0.004	9.46 ± 0.03	9.05 ± 0.08	-0.15 ± 0.03	0.27 ± 0.08	
GB6J225858+020340	2.67	0.329	18.77	301	5492 ± 370	3097 ± 492	46.502 ± 0.004	44.893 ± 0.010	47.155 ± 0.004	9.54 ± 0.06	8.97 ± 0.14	-0.48 ± 0.06	0.09 ± 0.14	
GB6J231104+342504	1.82	0.400	18.34	994	4140 ± 274	3871 ± 364	46.244 ± 0.012	44.496 ± 0.010	46.897 ± 0.012	9.15 ± 0.06	9.02 ± 0.09	-0.36 ± 0.06	-0.23 ± 0.09	
GB6J231449+020146	4.11	0.267	19.59	84	3975 ± 395	2903 ± 267	46.307 ± 0.010	45.164 ± 0.013	46.960 ± 0.010	9.15 ± 0.08	8.81 ± 0.09	-0.29 ± 0.08	0.05 ± 0.09	
GB6J231454+322439	2.84	0.344	19.17	115	4623 ± 479	3097 ± 404	46.578 ± 0.005	45.036 ± 0.010	47.232 ± 0.005	9.43 ± 0.08	9.01 ± 0.12	-0.30 ± 0.09	0.12 ± 0.12	
GB6J232228+184325	1.73	0.186	18.32	322	4295 ± 183	3871 ± 917	46.235 ± 0.021	44.941 ± 0.015	46.888 ± 0.021	9.18 ± 0.04	9.02 ± 0.27	-0.39 ± 0.04	-0.23 ± 0.27	
GB6J232235+081205	2.09	0.308	18.31	857	4295 ± 124	4838 ± 398	46.494 ± 0.005	44.863 ± 0.008	47.148 ± 0.005	9.32 ± 0.03	9.35 ± 0.07	-0.27 ± 0.03	-0.30 ± 0.07	
GB6J232733+094009	1.84	0.223	17.89	643	3776 ± 75	7935 ± 431	46.295 ± 0.009	44.361 ± 0.009	46.948 ± 0.009	9.10 ± 0.02	9.68 ± 0.05	-0.25 ± 0.02	-0.83 ± 0.05	
GB6J233013+334832	1.81	0.451	19.02	442	3988 ± 820	3677 ± 429	46.165 ± 0.015	44.681 ± 0.012	46.818 ± 0.015	9.08 ± 0.11	8.94 ± 0.10	-0.36 ± 0.11	-0.22 ± 0.11	
GB6J233620+064045	2.91	0.380	19.84	135	4666 ± 191	5806 ± 335	46.450 ± 0.007	44.928 ± 0.008	47.103 ± 0.007	9.37 ± 0.04	9.49 ± 0.05	-0.36 ± 0.04	-0.48 ± 0.05	
GB6J235758+140205	4.35	0.191	20.43	78	3182 ± 124	7161 ± 305	46.267 ± 0.015	44.327 ± 0.017	46.920 ± 0.015	8.94 ± 0.04	9.57 ± 0.04	-0.12 ± 0.03	-0.75 ± 0.04	
GB6J235829+043017	2.30	0.216	19.13	325	3151 ± 170	2129 ± 195	46.301 ± 0.008	44.811 ± 0.010	46.955 ± 0.008	8.95 ± 0.05	8.54 ± 0.08	-0.09 ± 0.05	0.32 ± 0.08	

This paper has been typeset from a $\text{\TeX}/\text{\LaTeX}$ file prepared by the author.